

POLITECNICO DI TORINO

Master of Science in Civil Engineering

Master's Thesis

Influence of soft inclusions on the fracture behaviour of cement paste



Polytechnic of Turin advisors:

Prof. Paola Antonaci
Eng. Giovanni Anglani

Candidate:

Luca Mercuri

TU Delft thesis advisors:

Prof. Erik Schlangen
Dr. Branko Šavija
MSc Claudia Romero Rodriguez
Ir. Emanuele Rossi



Hosting Institution:

**Delft University of Technology - Faculty of Civil
Engineering and Geosciences - Microlab**

July 2019

Abstract

Soft inclusions, such as capsules and other particulate admixtures are increasingly being used in cementitious materials for functional purposes (i.e. self-healing and self-sensing of concrete). Yet, their influence on the fracture behaviour and mechanical properties of the material is sometimes overlooked and requires in-depth study for the optimization of mechanical and/or smart properties.

An experimental investigation is presented herein on the role of bacteria-based lactate-derived particles on the fracture behaviour of cement paste in tensile configuration. These admixtures are currently used for the purpose of self-healing.

In order to understand the role of soft inclusions inside the cement paste different laboratory tests have been planned. The main mechanical properties such as the tensile strength, the work of fracture and the element stiffness were measured through the uniaxial tensile test (UTT). Then other tests and analysis have been performed to help data interpretation, digital image correlation was used to obtain strain contours on the surface of the samples during the tensile test, nanoindentation was used to measure micromechanical properties of cement-polymer interface, isothermal calorimetry tests have been performed to record the heat of hydration generated by the reaction between the different reactivities polymer with cement paste, computer tomography scans (CT scan) have been made to detect the effective position of healing agent particles inside the cement matrix before the UTT test in order to provide data for future lattice simulations. The influence of hydration age, dosage and different reactivity of soft particles addition into the samples were investigated.

Contents

1	Introduction.....	3
1.1	Self-healing and research background	3
1.2	Research scope and objectives	6
1.3	Research methodology	6
2	Literature survey.....	8
2.1	Self-healing in concrete	8
2.2	Autogenous self-healing	9
2.2.1.	Swelling of the cement matrix.....	9
2.2.2.	Un-hydrate cement and crystallization of calcium carbonate	9
2.2.3.	Mechanical causes.....	10
2.3	Autonomous self-healing.....	11
2.3.1.	Encapsulation	11
2.3.2.	Vascular healing.....	11
2.3.3.	Bacterial healing	11
2.4	Fracture in cementitious materials.....	15
3	Material and test methods.....	17
3.1	Materials	17
3.2	Experimental methods.....	20
3.3	Bond strength	20
3.3.1.	Sample preparation	21
3.4	Nanoindentation.....	23
3.4.1.	Sample preparation	25
3.5	Uniaxial tensile test.....	26
3.5.1.	Sample preparation	28
3.6	Digital image correlation.....	31
3.6.1.	Operating principle.....	31

3.6.2.	Sub-regions deformation.....	32
3.6.3.	Correlation criteria	33
3.6.4.	Strain computation.....	34
3.7	Isothermal calorimetry	35
3.7.1.	Sample preparation	35
4	Results and discussion	36
4.1	Bond strength of polymer-cement matrix interface	36
4.2	Micromechanical properties of the HA-Cement paste interface	38
4.3	Isothermal calorimetry	43
4.4	Boundary conditions of UTT	45
4.5	Influence of hydration age on the mechanical properties	48
4.6	Influence of HA dosage on the mechanical properties	50
4.7	Influence of polymer reactivity on mechanical properties	52
5	Conclusions and future developments.....	54
6	References	55

1 Introduction

1.1 Self-healing and research background

Structural materials properties have been considerably improved in every aspect. In the past the product was evaluated on the resulting performance without knowing what were the internal changes of the material that caused improvements: developments were linked to a slow trial and error process [1].

The major contributions are to be attributed to study and research of last two centuries. Two factors mainly contributed to the development:

- The notion that microstructure in combination with physicochemical techniques determines material properties;
- The availability of (semiempirical) models linking the microstructure to the final material properties and vice versa.

Research and experimentation in this direction has led to materials design, today material properties can be regulated precisely in order to fit the function they have to perform.

For safety and economic reasons many efforts have been done on durability and damage prevention, i.e. the materials are designed and prepared in such a way that the deterioration is postponed as much as possible [1].

Durability is defined as the ability of a material to remain serviceable in the surrounding environment during the service life without damage or unexpected maintenance. Durability depends on various factors such as the environmental conditions, climate and season, technical performance of the product and many others [2].

In recent years to make materials effectively stronger and more reliable it has been realized that an alternative strategy can be followed for example by providing a built-in capability to repair the damage incurred during use. These man-made materials are called self-healing materials and are able to repair structural damage autogenously or with the help of an external stimulus.

Self-healing property is a relatively new area of materials research and one of the promising application fields of nanotechnology especially because defects generally emerge at a very small scale and healing presupposes the presence of defects.

Self-healing materials are the answer to the impossibility to face the Damage Prevention paradigm. In fact, this paradigm states that, a material designed to have microstructure opposing micro-cracks formation or extension with "few" and "very small" defects, can become so strong that the load level necessary to create damage will never be reached.

The concept of Damage Management is introduced in the book *Self-Healing Materials*, which forms the basis of the field of self-healing materials [1]. This paradigm, on the contrary, assumes that damage is not a problem as long as there is a mechanism for recovering that balances the system.

Currently there are several areas in materials engineering where this new self-healing technology is applied such as in polymers, composites, cementitious materials, in asphalt mixtures or in aluminum alloys.

Concrete is used as main material for buildings and infrastructures. It is in fact a favorable construction material due its production process, raw material availability and compression strength characteristics.

In the last twenty years, there was a growing interest in the scientific community [3] regarding self-healing concrete as visible in Fig. 1.

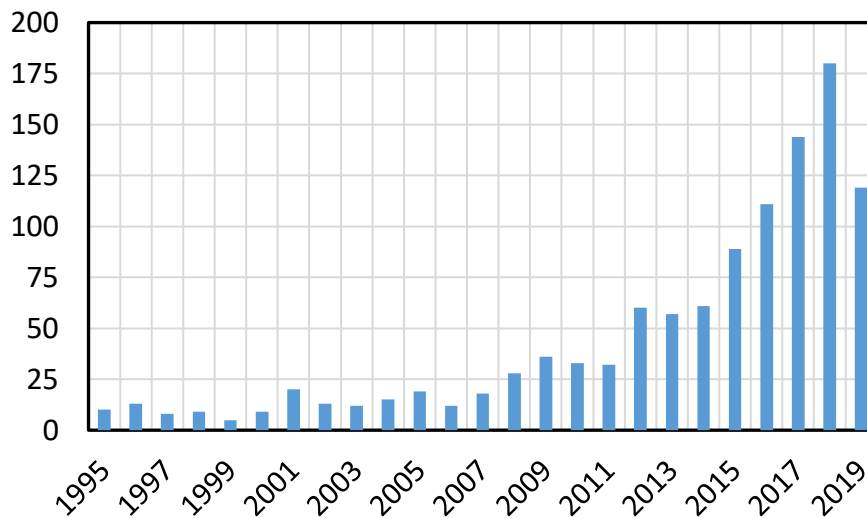


Fig. 1. Number of publications per year. Science direct search with key words “self” AND “healing” AND “concrete” [3].

In fact, improving service life of concrete structures will reduce risks and consequently demand for new structures [4]. This, results in the use of less raw materials and a reduction in energy consumption, pollution and CO_2 production. Data from worldwide show the enormous amounts of money spent by society due to the lack of quality and durability of concrete structures.

A report on the condition of the United States infrastructure systems has been published from the American Society of Civil Engineers (ASCE) [5] Fig. 2. Only for bridges one in nine of nation’s bridges are structurally deficient or functionally obsolete and the

average age of the nation’s 607,380 bridges is currently 42 years old. It is estimated that to eliminate all bridges deficiencies by 2028 it would need to invest \$20.5 billion annually, while \$12.8 billion is being spent for basic expenses.

Category	1988*	1998	2001	2005	2009	2013
Aviation	B-	C-	D	D+	D	D
Bridges	-	C-	C	C	C	C+
Dams	-	D	D	D+	D	D
Drinking Water	B-	D	D	D-	D-	D
Energy	-	-	D+	D	D+	D+
Hazardous Waste	D	D-	D+	D	D	D
Inland Waterways	B-	-	D+	D-	D-	D-
Levees	-	-	-	-	D-	D-
Public Parks and Recreation	-	-	-	C-	C-	C-
Rail	-	-	-	C-	C-	C+
Roads	C+	D-	D+	D	D-	D
Schools	D	F	D-	D	D	D
Solid Waste	C-	C-	C+	C+	C+	B-
Transit	C-	C-	C-	D+	D	D
Wastewater	C	D+	D	D-	D-	D
Ports	-	-	-	-	-	C
America's Infrastructure GPA	C	D	D+	D	D	D+
Cost to Improve	-	-	\$1.3 trillion	\$1.6 trillion	\$2.2 trillion	\$3.6 trillion

Fig. 2. Costs to improve performance level. United States infrastructure systems condition report published from the American Society of Civil Engineers (ASCE) 2013 [5].

Costs needed to improve infrastructures performance increase with time because of demand for new infrastructures and aging of existing ones Fig. 2.

Moreover, indirect costs due to traffic interruptions and associated lost productivity should not be overlooked because they are higher than the direct cost of maintenance and repair [6], [7].

In the Netherlands one third of the annual budget for large civil engineering works is spent on inspection, monitoring, maintenance, upgrading and repair [8]. In the United Kingdom repair and maintenance costs account for over 45% of the UK’s annual expenditure on construction [9].

Improve durability and longevity of the structures it’s a severe environmental and economic issue on which research is focusing. For concrete structures self-healing technology seems to be a good strategy to mitigate the direct and indirect costs related to repair of cracked concrete elements. Many types of self-healing (SH) technology have been investigated in the past 20 years [10] [11] and capsules in particular demonstrated to be an efficient way to face the issue of protecting the healing agent prior to cracking while

at the same time allowing the triggering of the healing mechanisms [10] [12] [13] [14] [15]. Despite the great interest shown on this technology, there are still relatively few studies concerning the effects that these particles have on the mechanical properties of the cementitious composites.

1.2 Research scope and objectives

The durability issue is the main reason why many research projects, included this master thesis project, have started. The study focuses on the role of soft inclusions (healing agent particles) on mechanical behavior of cement paste samples during uniaxial tensile test. Three types of industrially made particles are used.

The particles are composed of lactate bio-polymer, a calcium source and bacterial spores (of *Bacillus cohnii*-related strains).

The scope of the project is to try to develop design considerations based on experimental results. The objectives to reach the research scope are the following:

- Develop a methodology to evaluate qualitatively and quantitatively how capsules influence the fracture process on cement;
- Provide experimental data for cement paste with capsules inclusions (that are not available in literature) for the lattice model and for successive studies;

1.3 Research methodology

To understand the influence of healing agent on cement paste samples different laboratory tests have been planned. Three main representative quantities have been measured through the uniaxial tensile test:

1. One fracture mechanics property: work of fracture (W_f);
2. Two mechanical properties: tensile strength (σ_t) and element stiffness (K_e).

The tests have been performed changing three influential parameters:

- A. Reactiveness;
- B. Quantity;
- C. Hydration age.

Uniaxial tensile tests besides measuring the influence of hydration, quantity and reactivity on the composite material, was useful to measure bond strength between the polymer material of which inclusions are composed, and cement paste.

Other test such as Nano-indentation, isothermal calorimetry or CT-scan analysis will be supportive for results interpretation.

2 Literature survey

2.1 Self-healing in concrete

Cracks are intrinsic concrete characteristics and their morphology allow the ingress of aggressive gasses and liquids that can endanger the durability of a structure [16] [17] [18]. Usually the problem can be temporally stemmed by applying manual repair. But cracking can occur at any stage of concrete service life moreover early micro-cracks are extremely difficult to detect due to their size. For those reasons, and many others, planned manual maintenance may not be effective, especially for cracks that are formed in early ages. To avoid that scientists inspired by nature have created self-healing concrete able to self-repair.

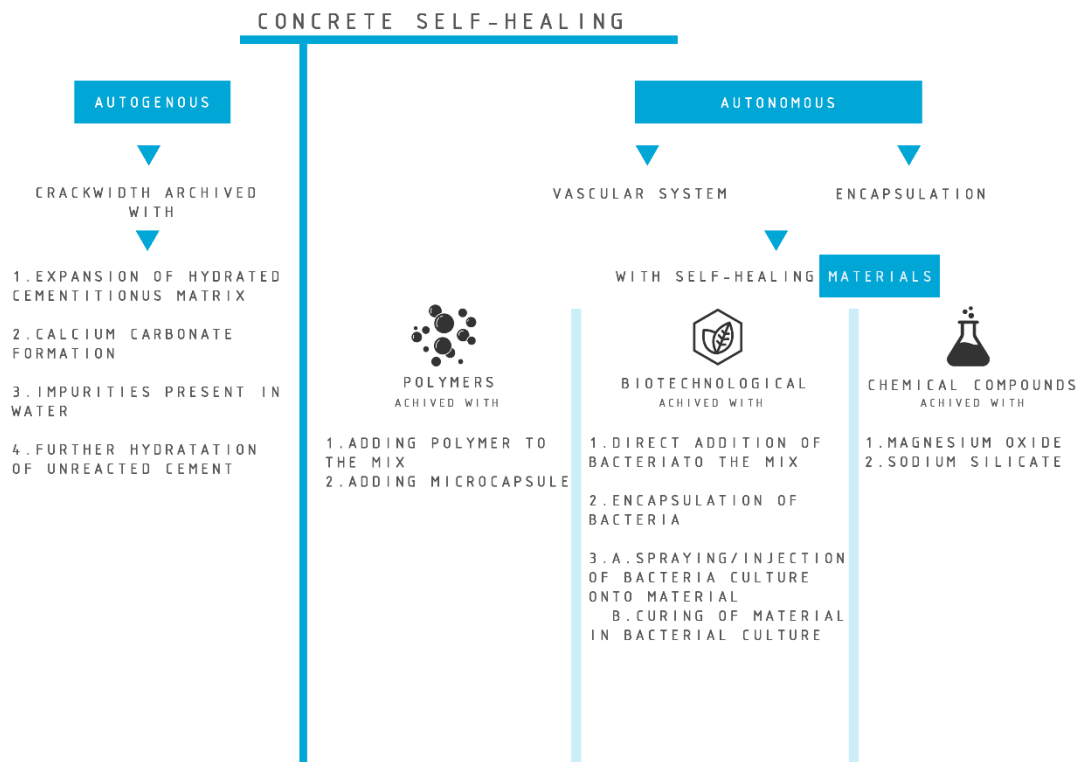


Fig. 3. Autogenous and autonomous self-healing in concrete.

Various research groups have studied different self-healing concepts over the last decade. One of the first to study crack healing in polymers was Malinskii in 1973 [19]. In the following years the phenomenon attracted further study and experimentations on many types of material including concrete [20].

It is possible to divide concrete self-healing into two main groups (Fig. 3): autogenous and autonomous [21].

Autogenous self-healing means the healing process triggered without the need of any external operation while autonomous self-healing is developed by adding admixtures for healing purposes [4]. Fig. 3 shows schematically the main aspects of both groups.

2.2 Autogenous self-healing

Recovery against environmental action is strictly related to narrowing of crack width with time. It is possible to distinguish three causes for this to occur: physical, chemical, and mechanical Fig. 4.

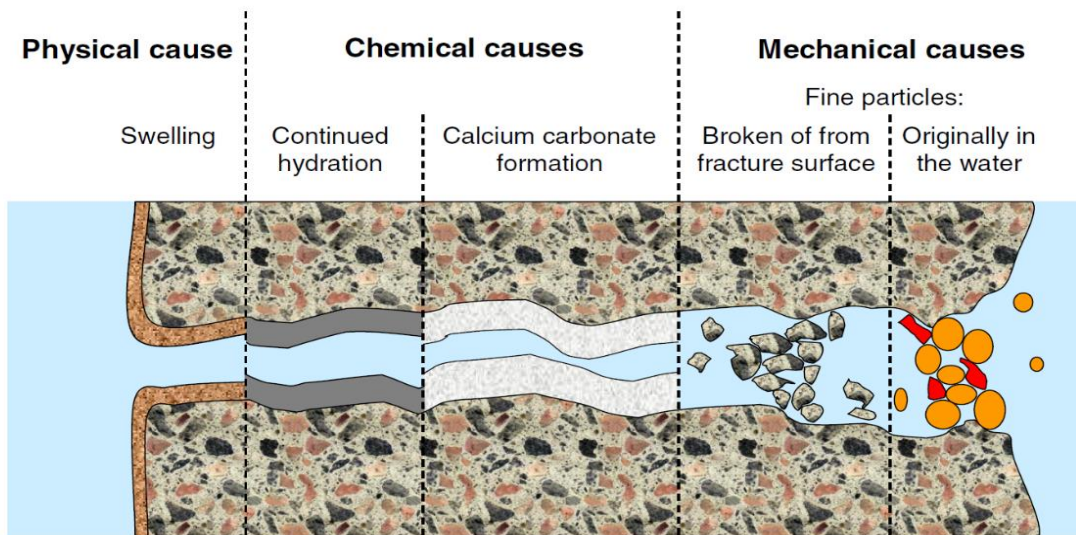


Fig. 4. Causes of autogenous self-healing in concrete. M. de Rooij et al. (Eds.): Self-Healing Phenomena in Cement-Based Materials, RILEM 11, pp. 65–117. DOI: 10.1007/978-94-007-6624-2_3. [22].

2.2.1. Swelling of the cement matrix

The swelling of hydrated cement paste into the crack faces can be classified as physical cause. The effect of swelling is marginal when estimated it cause a reduction of the fluid flow by less than 10% [22].

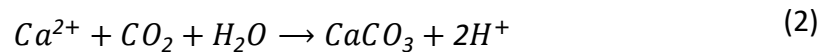
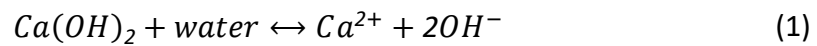
2.2.2. Un-hydrate cement and crystallization of calcium carbonate

Two chemical process can heal concrete cracks: one concerns the hydration of cement which has not reacted, the other concerns the formation of calcium carbonate and the crystals growth on the crack faces.

The first one occurs because the products of hydration occupies more space than the reactants. When water from external environment meets unhydrated reactants, these start to react filling the free spaces that are represented by the crack. Hydration of unreacted cement combined with other actions like swelling, can repair small cracks width of 0.1 mm [22]. This mechanism is no more relevant after few years, Neville [23] associates the benefits of continuing hydration only for concretes in their early ages, whereas calcium carbonate crystallization can be more important in later ages.

Studied by Edvardsen the second reaction is the most efficient to heal the crack [24]. Calcium hydroxide contained in cement react with carbon dioxide CO_2 from the atmosphere or dissolved in water to form calcium carbonate.

The reaction depends on solution pH, temperature and reactants concentration [25]. It occurs when the H_2O and CO_2 from external environment enter into the crack forming CO_3^{2-} in solution, that react with Ca^{2+} ions from the pore water Equation (1). The resulting $CaCO_3$ precipitate and fill the crack Equation (2).



From thermodynamic considerations the precipitation of $CaCO_3$ can be improved by:

- raising the temperature of the water;
- increase of the pH value of the water;
- partial fall of CO_2 in water.

2.2.3. Mechanical causes

Finally, two mechanical causes can heal the crack, both less reliable than the above mentioned because they depend on the geometry of the crack, the age and the presence of water.

2.3 Autonomous self-healing

Autonomous self-healing involves designed additives to be mixed in cementitious materials for the functional purpose of healing and use techniques to transport such additives. Admixtures such as fly ash or specific expansive agent are intentionally incorporated into concrete in advance.

2.3.1. Encapsulation

Encapsulation is one of the preferred techniques for the direct delivery of healing agents to the damaged area. Capsules have two main functions: the first one is to incorporate and isolate the healing agent (HA) from the concrete mix, the second one to release the HA when a crack pass through them.

Based on the report of Van Tittleboom [26] four fundamental steps must be considered when making healing with capsules:

- Survival to the mixing process;
- Influence on mechanical properties and workability;
- Compatibility with the healing agent and the cement matrix;
- Probability and release efficiency of the capsules and healable crack volume.

2.3.2. Vascular healing

Another method to deliver healing agents into the concrete specimen is the vascular approach; the method inspired from human vascular structure [27] [28] consists into a network of hollowed tubes embedded into the concrete structure created to let the healing agent flow inside; the system can transport single or multiple healing agents that are supplied externally [27], [29].

2.3.3. Bacterial healing

Bacteria are already employed in engineering to purify water and wastewater plants from chemical agents or for decontamination of soils [30].

Although the metabolic pathways of different bacteria can vary but the principle is essentially the same: a bio-based healing agent is incorporated into fresh concrete and when a crack appears in hardened concrete the bacteria become active, precipitate limestone and seal the open crack [4]. Bio-based self-healing efficiency can be measured in terms of water tightness regaining previously lost by cracking.

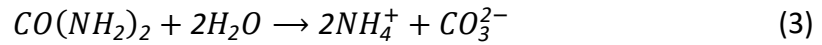
Biotechnological healing is categorized under the genus bacillus group of bacteria which are highly resistant to the alkaline environments [20], [31]. "Extremophilic bacteria" revealed themselves to resist in extreme environments; they can be found in deserts, rocks and also in ultra-alkaline environments that are comparable to that of internal concrete [20], [31], [32].

To ensure bacterial healing a source of nutrient must be provided, is then possible to obtain precipitated calcium carbonate as a result of the metabolic process.

Calcium carbonate production depend on the bacteria type:

- **Ureolytic Bacteria**

Sporosarcina ureae, *Sporosarcina pasteurii* (also named *Bacillus pasteurii*), *Bacillus sphaericus*, and *Bacillus megaterium* are some bacteria belonging to the Ureolytic group. These bacteria form $CaCO_3$ by decomposing urea into ammonium or ammonia and carbonate ions Equation (3) that combines with Ca^{2+} ions present in pore solution Equation (4).



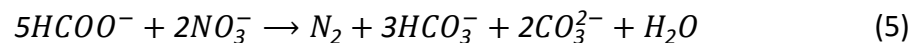
Several studies for waterproofing, strength and durability improvement of porous and cracked concrete are available in literature. Many author review pro and cons of using that kind of bacteria [33], [34], [35], [36], [37], [38].

For instance, Ureolytic bacteria activity is speeded up with the presence of the urease enzyme as a catalyst. In fact, from reactions above (Equation (3) and (4)) 1 mol of $CaCO_3$ can be formed if 1 mol of urea is supplied.

Without this enzyme the urea hydrolysis is always possible but with the catalyser enzyme the speed is 10^{14} times faster [10]. On the other hand, for a certain concentration of bacteria when the amount of urea exceeds a certain value a inhibitory effect is found. The same authors find that also, temperature affect precipitation efficiency: at lower temperatures, around $10 \text{ }^\circ\text{C}$, a significant reduction in precipitation rate $CaCO_3$ is recorded.

- **Denitrifying Bacteria**

$CaCO_3$ precipitation induced with bacteria through nitrate reduction can be achieved by *Diaphorobacter nitroreducens* or *Pseudomonas aeruginosa* Equation (5). For their suitability to function under oxygen limited conditions they have been tried successfully for self-healing concrete.



Bacteria under optimum conditions (pH value, adequate nutrients, immersed non-stop in water) were able to heal also crack width of $370 \pm 20 \text{ mm}$ in 28 days and $480 \pm 16 \text{ mm}$ in 56 days and regain water tightness up to 85 % [39], [40].

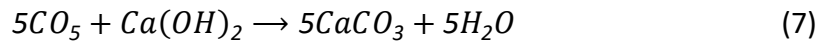
- **Calcium lactate-based bacteria**

To guarantee the precipitation of calcium carbonate bacteria need an organic substrate to convert metabolically into inorganic carbon that can react with free calcium to precipitate calcium carbonate.

Schlangen [41] and Jonkers [42], proposed lactate-based bacteria. The active metabolic conversion of calcium lactate provides a more efficient self-healing process in concrete. Jonkers [42] in particular proposed the employment of *Bacillus Pseudofirmus* and *Bacillus Chonii* a two-component bacteria healing agent plus calcium lactate directly added to the mix. From the experiments it was possible to see the catalyst action of bacteria transforming the lactate into calcium carbonate.



The quantity of calcium carbonate precipitate increased when the produced CO_2 reacted with the molecules of portlandite, as per the following carbonation reaction.



- **Zelfherstellend paviljoen (Self-healing pavilion)**

The promising results in laboratory-scale tests led to the experimentation on real scale with the construction of a concrete self-healing pavilion.

The structure is the result of the collaboration between the Department of Self-Healing Materials at Delft University and Marcus architects (Holland).

The use of bio-concrete reduces the amount of concrete required (60 mm thick concrete shell) and the CO_2 climate load. The building Fig. 5 represents a huge sustainable step for the most commonly used building material.



Fig. 5. Pavilion for the Rescue Brigade & First Aid at the recreational lakes, the Galderse Lakes, Breda. Realization of self-healing roof and facade shell for the first time in the world. Details on: <https://www.marcus-architecten.nl/012-paviljoen-reddingsbrigade-breda/>.

2.4 Fracture in cementitious materials

Regarding the study of self-healing technology, many efforts have been made towards the healing ability, the efficiency and the different functioning mechanisms; in literature, however, it is possible to notice a disproportion between the studies mentioned above and the influence of these admixtures into cementitious materials.

Most part of research concerning cracking in these materials is oriented towards the measure of the ability to regain water tightness (the ability to fill up the crack after it formed) and width reduction measurements; much less literature studies use fracture for the information that it brings on the post-peak phase of the breaking material.

Fracture mechanics applied to concrete design can provide much insight on how the size of structural element may affect the ultimate load capacity. Moreover, interpretation of crack propagation allows predictions on stability of the material in the softening phase. Le-Yang Lv and Hongzhi Zhang in [43] proposed a feasible approach for investigating the fracture and triggering behavior of self-healing microcapsules embedded in a cementitious system. The study provides a promising way to follow for the design of capsule-based self-healing cementitious composites and their optimization.

However, the authors note that some improvements are needed; for instance, a better procedure for bond strength measurements, a better control of boundary conditions during the tensile test and to establish an appropriate relationship between local hardness and fracture strength of the cement paste.

Wolski and Landis in [44] conducted three-dimensional imaging experiments with small cylinder specimens subjected to split test (brazilian tensile test). Using synchrotron-based x-ray microtomography they realized 3D images while the specimen under load was varying damage degrees.

There are numerous advantages of an in-situ arrangement, multiple scans can be made on the same specimen subject while it is under load, allowing measurements of changes in the internal structure. To measure the energy required for crack growth, the authors employed a technique previously presented by Landis et al. [45], G_f was measured with the direct energy released U divided by the crack area A created during the loading process:

$$G_f = \frac{\Delta U}{\Delta A} \quad (8)$$

ΔA is measured from the 3D image data: previously the undamaged specimen is segmented into void and solid then, a connectivity analysis is run to highlight the crack

surfaces, for each damage steps. ΔA is simply the difference between the total surface area measured in two successive scans.

The authors note that one of the limits of this approach is represented by the maximum resolution achievable by the synchrotron to measure crack surface area and confirm that X-Ray CT is a powerful tool to investigate cracks morphology. Moreover in-situ measurement considerably limits the size of the testing samples, for that study *5 mm* diameter samples where used.

3 Material and test methods

3.1 Materials

Cement pastes were prepared by mixing ordinary Portland cement (OPC) CEM I 52.5 R and tap water with water-to-cement ratio (w/c) of 0.45, compliant with European standard EN-197-1 [46]. The healing agent (HA) particles were added to the paste specimens in dosage of 1.3% by weight of cement, which resulted in 1.5 % by volume of composite. The particles were composed of lactate bio-polymer, a calcium source and bacterial spores (of *Bacillus cohnii*-related strains). The activation nutrients were obtained from Basilisk (Self-healing capsules, The Netherlands) [47]. Three polymer types were initially investigated, named L (low), M (medium) and H (high). Raw materials for their production were the same according to the supplier but each polymer underwent different production process resulting in different levels of chemical and physical interaction in the alkaline environment of the cement paste.

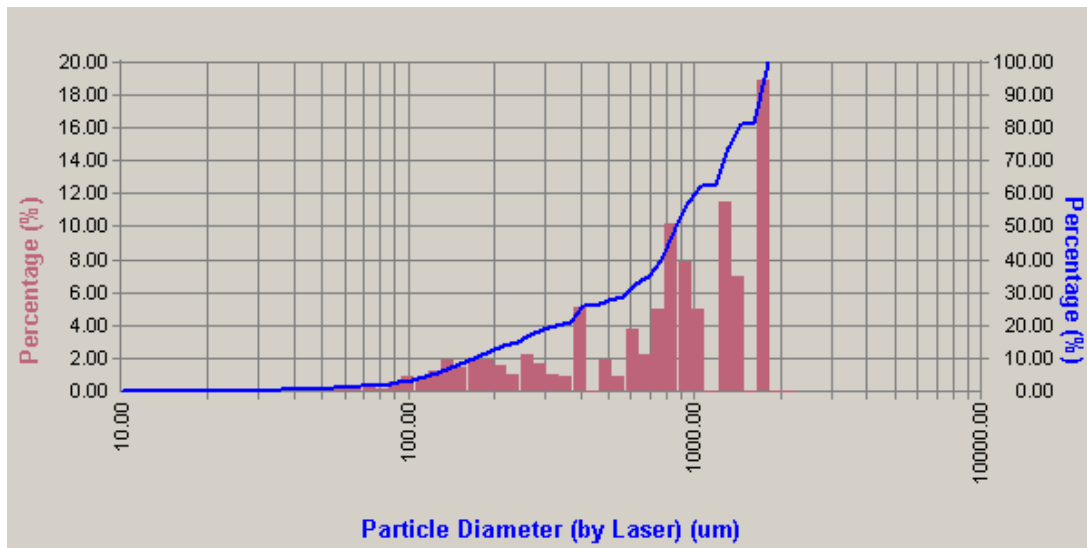


Fig. 6. Particle diameter for the L reactivity polymer. Diameters measured with DIPA - 2000 (Donner Technologies).

From volume measurements DIPA - 2000 (Donner Technologies) can calculate particles diameters. Fig. 6 shows the histogram in pink and the cumulative curve in blue of low reactivity polymer. The mean diameter calculated is $416.86 \mu m$; the control diameters are $D_{10}: 49.79 \mu m$, $D_{50}: 194.83 \mu m$, $D_{90}: 1213.38 \mu m$.

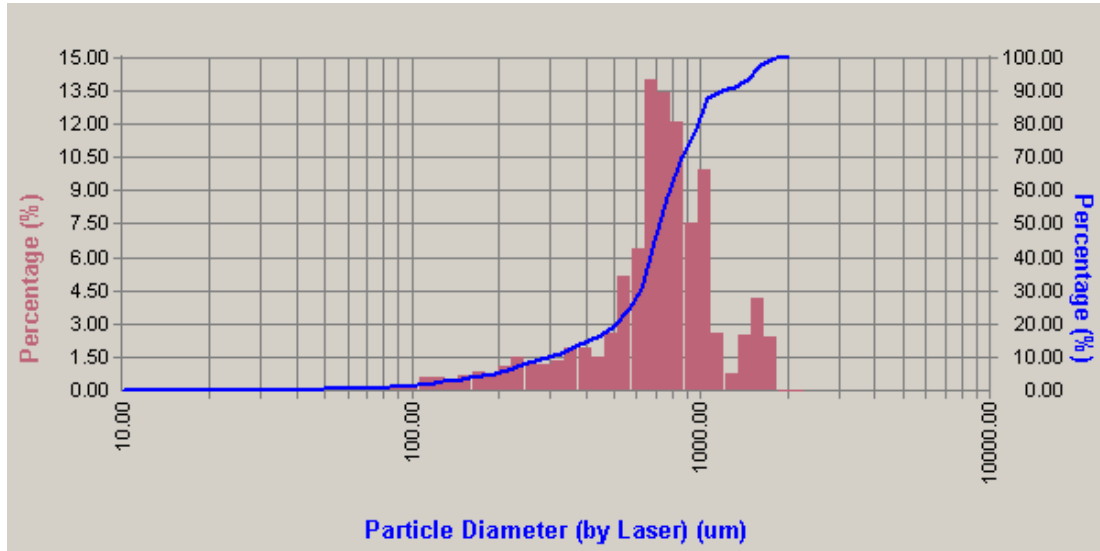


Fig. 7. Particle diameter for M reactivity polymer. Diameters measured with DIPA - 2000 (Donner Technologies).

For the medium reactivity polymer, the particle diameters are shown in Fig. 7. It is possible to see the histogram in pink and the cumulative curve in blue. The mean diameter calculated is $513.26 \mu m$; the control diameters are D10: $86.59 \mu m$, D50: $534.71 \mu m$, D90: $940.61 \mu m$.

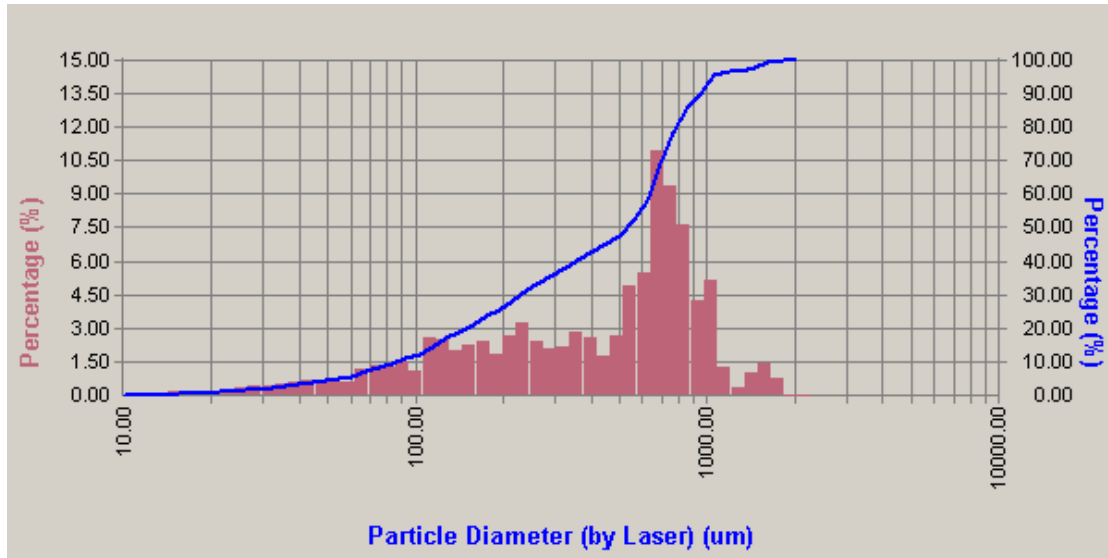


Fig. 8. Particle diameter for H reactivity polymer. Diameters measured with DIPA - 2000 (Donner Technologies).

For the high reactivity polymer, the particle diameters are shown in Fig. 8. It is possible to see the histogram in pink and the cumulative curve in blue. The mean diameter calculated is $299.53 \mu m$; the control diameters are D10: $64.69 \mu m$, D50: $208.30 \mu m$, D90: $762.05 \mu m$.

In Fig. 9 (a), (b), (c) the three kind of particles are shown.



Fig. 9. In the first picture (a) low reactivity particles, in (b) the medium and in (c) the high.

3.2 Experimental methods

In order to understand the role of soft inclusions inside the cement paste different laboratory tests have been planned. The main mechanical properties such as the tensile strength σ_t , the work of fracture W_f and the element stiffness K_e have been measured through the uniaxial tensile test (UTT). Then other tests and analysis have been performed to help data interpretation, in particular, uniaxial tensile test has been coupled with digital image correlation (DIC) to obtain strain contours on the surface of the samples during the test; nanoindentation has been coupled with scanning electron microscope (SEM) analysis in backscattering mode (BSE) to correlate the micromechanical properties to the chemical composition of cement-polymer interface; isothermal calorimetry tests have been performed to record the heat of hydration generated by the reaction between the different reactivities polymer with cement paste; computer tomography scans (CT scan) have been made to detect the effective position of healing agent particles inside the cement matrix before the UTT test in order to provide data for future lattice simulations.

3.3 Bond strength

To measure the bond strength between the material composing the healing capsules and the cement paste bi-material Fig. 10 samples have been prepared and tested under uniaxial tensile regime.

The tests were carried out in displacement control with the mini tension-compression machine showed in Fig. 10 with load cell of 500 N .

The samples were glued to the loading plates which were connected to the frame through hinges, therefore allowing bending stresses. The test was performed in displacement control at a rate of $0.5\ \mu\text{m}/\text{sec}$. The bond strength was calculated from the measured peak load.

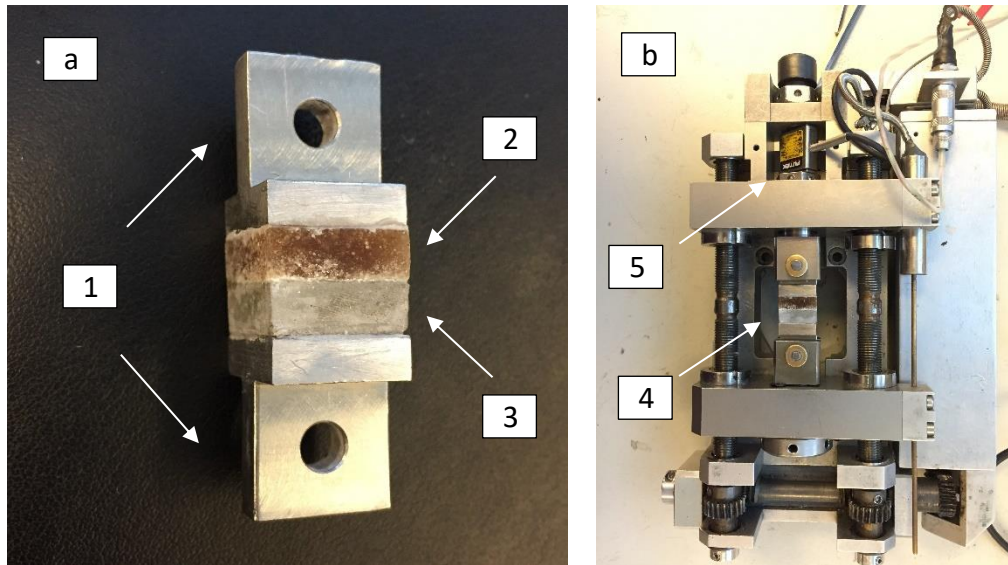


Fig. 10. Here 28 days old sample. In (a) Bi-material sample glued to the testing hinged plates (1), with the polymer on the upper layer (2) and cement paste on the lower one (3). In (b) Mini tension compression machine with unbroken sample (4); 500 N load cell (5).

3.3.1. Sample preparation

The bi-material samples consist on square prisms shaped samples with equal parts of biopolymer and cement paste.

The whole sample dimensions are $15\text{ mm} \times 15\text{ mm} \times 10\text{ mm}$. For the preparation of the polymeric part, previously crushed healing agent particles were placed inside a shallow circular mold and heated to the corresponding transition temperature (T_G). The T_G was different for each polymer and was determined by trial and error as the temperature at which the polymer became homogeneous without suffering thermal degradation. In fact, when the heating temperature was too low only the surface particles melted whereas internally only the grain limbs melted. On the other hand, when the heating temperature was too high air bubbles formed and parts of the polymer presented darkened areas. To prevent air bubbles and too high transition temperatures a constant pressure of 15.4 kPa was applied using a pre heated weighted mass Fig. 11. Table 1 shows the temperatures at which each studied polymer was heated. After cooling, the polymer regained its original rigidity and was ready to be cut.

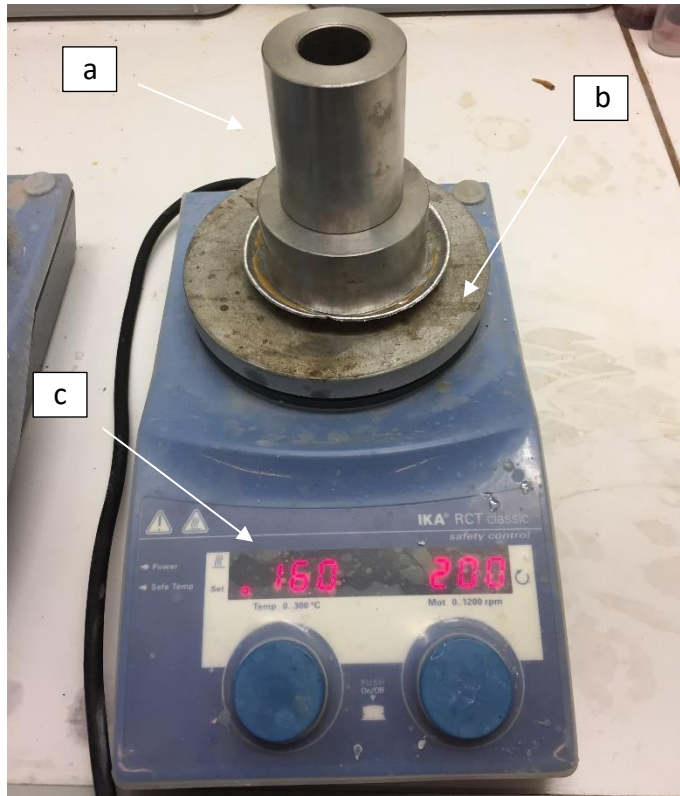


Fig. 11. Preparation of healing agent layer for bond strength test; the constant pressure is applied through the cylindrical mass (a) on the top of the heating plate (b). In (c) the indicator of temperature in degree Celsius.

For each polymer, 5 samples were prepared as follows.

The polymeric half was placed into a custom-made mold and the same volume of cement paste was poured to fill the other half.

Low	Medium	High
175 ±5 °C	165 ±5 °C	145 ±5 °C

Table 1. Transition temperatures

The samples were left wrapped for 24 h, to not vary the internal water cement ratio, at laboratory conditions and then demolded. After demolding only samples that were not de-bonded were half wrapped (on the polymer side) and cured in a chamber at 20 °C and 95 % of relative humidity until the age of 28 days. Only the polymer side were wrapped because of high sensitivity to contact with water which causes it to swell. The cement side instead had to stay in contact with the humidity of the external environment to avoid drying and follow the same process of the notched samples.

In Fig. 12 the resulting biomaterial samples are shown. High reactivity polymer samples de-bonded from cement paste after demolding and therefore the bond strength was considered nil.

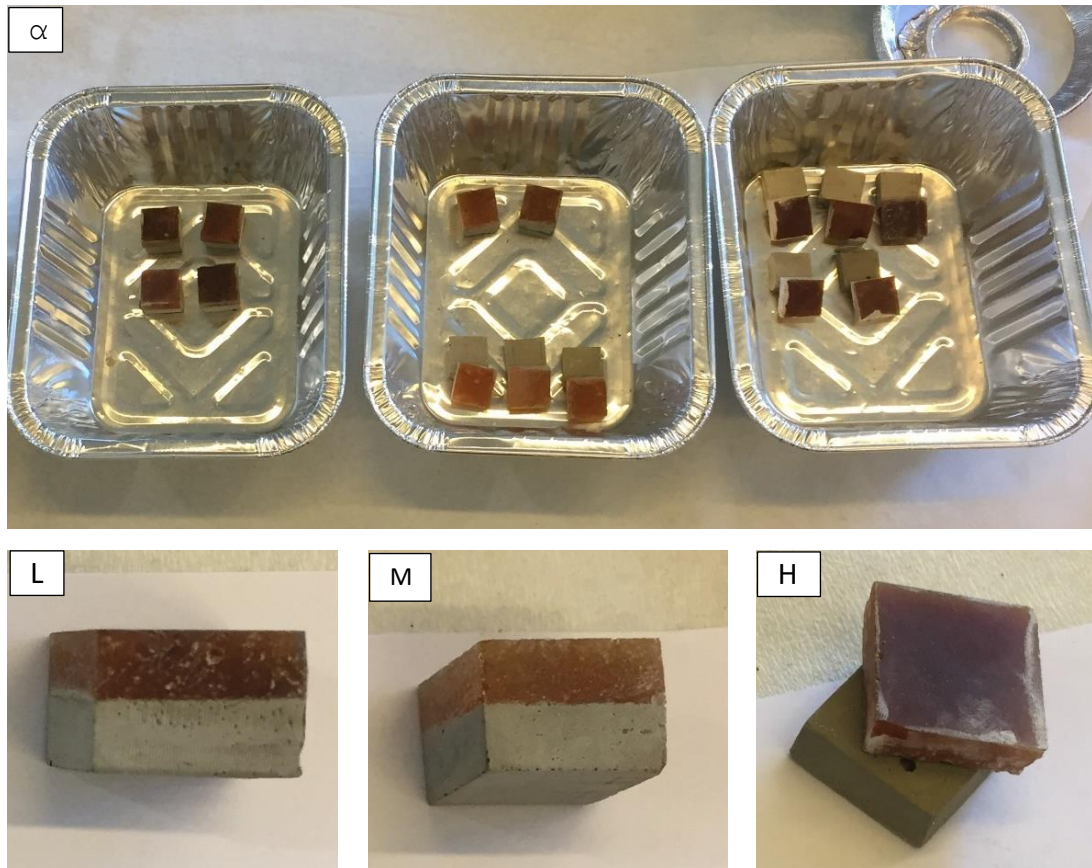


Fig. 12. Here 48 h old samples. On the left in (α) is possible to see that the samples from the batch with L polymer are fully bonded to the cement layer, in (L) a closer look; the batch in the center of (α) is the one with M polymer and only two on five samples are bonded to the cement part, in (M) a closer look; on the right in (α) there is the H polymer and all five samples decoupled from the cement part, in (H) a closer look;

3.4 Nanoindentation

Theoretical and experimental progress in Nano mechanics opens new views in materials science in general. Cement-based composites benefited it, in fact it becomes possible to identify the mechanical effects of the elementary chemical components of cement-based materials. In the last years micromechanical properties of the four clinker phases, of portlandite, and of the C-S-H gel can be measured through nanoindentation.

Agilent Nano Indenter (G200, Keysight, USA) with a diamond Berkovich tip from TU-Delft Microlab was used to measure the local micromechanical properties of the interface

between the polymeric inclusion and the cement matrix. A grid of 5×20 for a total of 100 indents was performed to measure the E modulus and hardness.

Using the continuous stiffness method (CSM) developed by Oliver and Pharr [48] the average modulus and hardness are obtained as a continuous function of the depth of surface penetration. To ensure the accuracy of measurements the quartz standard was indented before each test.

The surface approach velocity was 10 nm/s and the limit for indentation depth was fixed at 100 nm . For each polymer type two samples containing SH inclusion were prepared.

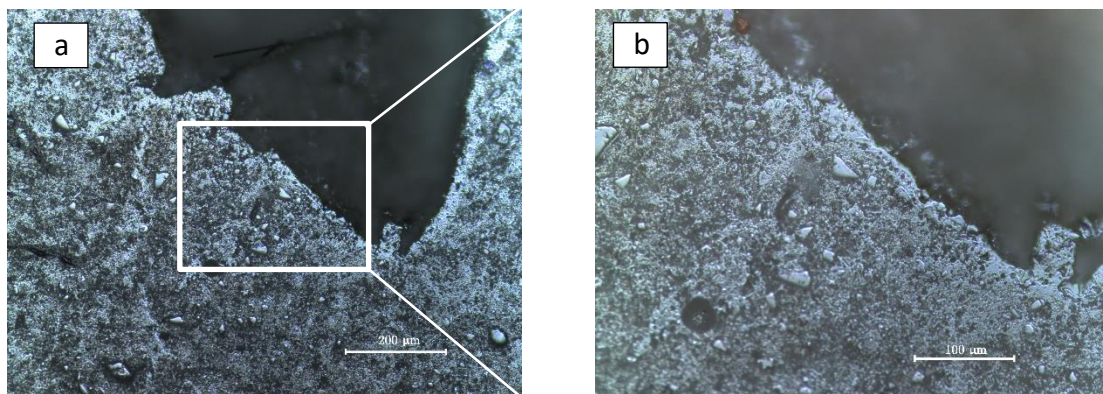


Fig. 13. In (a) is possible to see the images taken with the optical microscopy of the indented zone; in (b) the indented area is enlarged.

On the first set more as a trial a shorter strip length 5×10 indents for a total length of $90 \mu\text{m}$ was performed. The second with 5×20 indents for a total length of $190 \mu\text{m}$ confirmed the results obtained from the first set.

The strips start from the edge of cement matrix, the interface between polymer and cement. The indented sections presented an edge because of the void left by the ejected inclusion during the specimens' preparation.

In this research, the minimum sampling number for statistical confidence of results was not considered. The rectangular matrix with $10 \mu\text{m}$ separation between each indent was performed. After the test, the surface of sample was analyzed with SEM in backscattering mode (BSE) to correlate micromechanical properties with chemical composition of the indented area.

The projected area of contact for a Berkovich indenter is:

$$A = 24.5 h^2 \quad (9)$$

the semi-angle for an equivalent conical indenter is 70.3° .

3.4.1. Sample preparation

Nanoindentation tests were performed for specimens after 38 days as follow. After 28 days of curing at 20 °C and 95 % of relative humidity discs of thickness equal to $3 \pm 0.5 \text{ mm}$ were cut from the cylindrical samples $r = 5 \text{ cm}$, $h = 10 \text{ cm}$ containing HA inclusions; the same day they were immersed for 7 days into isopropanol solution to stop the hydration.

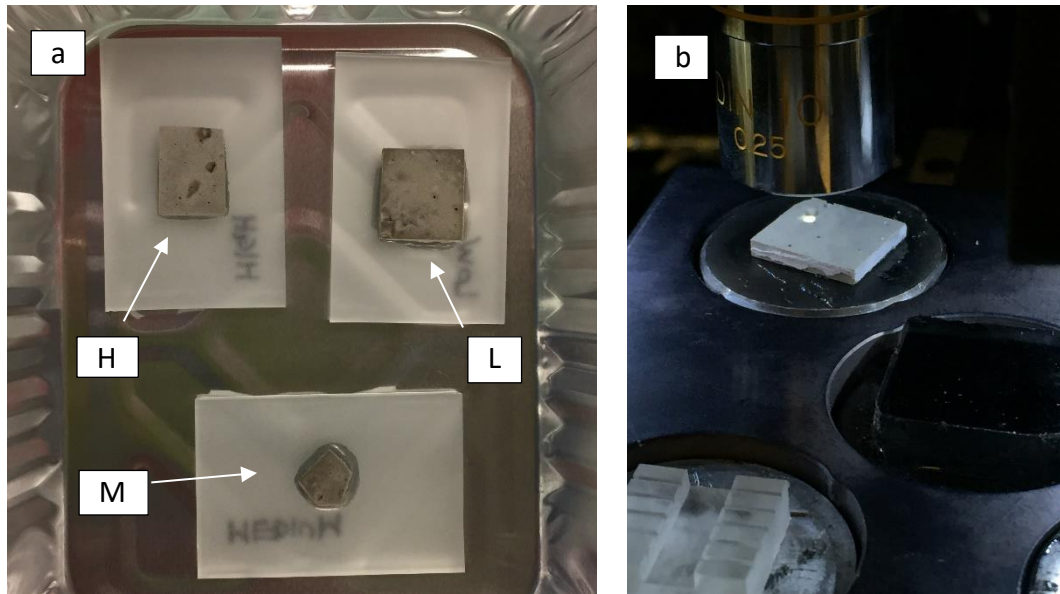


Fig. 14. Samples after grinding and polishing (a). In (b) sample *L* before nanoindentation test.

The volume of isopropanol used was 100 times that of the paste in order to facilitate solvent exchange. For an optimal removal of the water, the solvent has been changed twice during the first 24 hours [49].

The following step was vacuum drying in a desiccator for 1 day. The samples were glued onto a glass holder and then they were ready to be grinded and polished, this operation required 2 days. The specimens were ground using abrasive paper with grain size (European P-Grade) *P 800* (5 min), *P 1200* (10 min) during which ethanol was used as a cooling liquid. After grinding, samples were polished with diamond paste $6 \mu\text{m}$ ($25 \pm 5 \text{ min}$), $3 \mu\text{m}$ ($25 \pm 5 \text{ min}$), $1 \mu\text{m}$ ($25 \pm 5 \text{ min}$).

Between each grinding and polishing step, samples were soaked into an ultrasonic bath to remove the residual particles on the sample surface formed during the process. Immediately after sample preparation the samples were tested with nanoindenter to avoid carbonation of the tested surface.

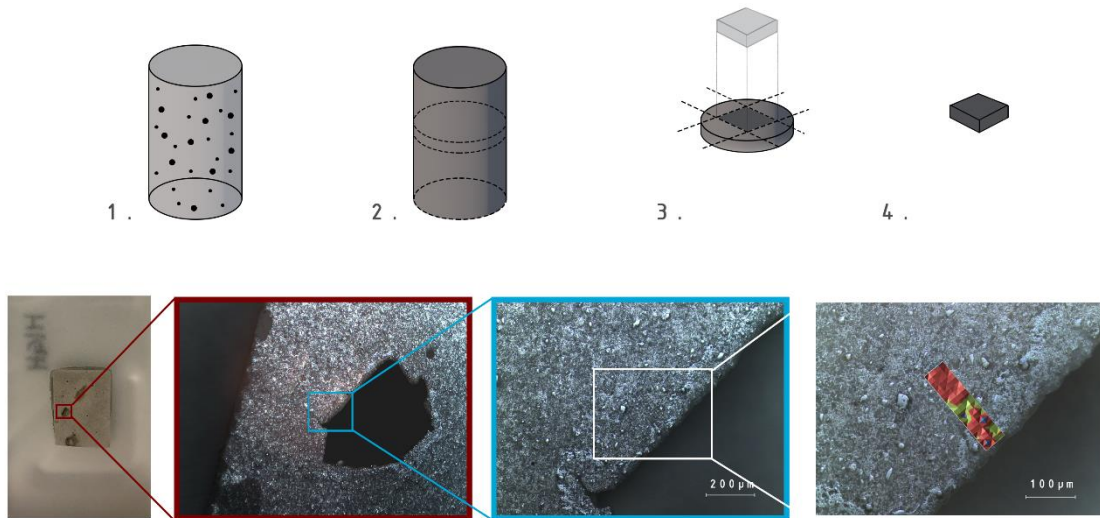


Fig. 15. Scheme of sample preparation steps for nanoindentation test; from the cylinder block (1) to the indented area results.

3.5 Uniaxial tensile test

The Uniaxial tensile test (UTT) was performed by means of a servo hydraulic press Axial Tension-Compression Systems, model 8872 from Instron (High Wycombe, UK) on 6 samples per batch, 10 batches for a total of 60 UTT tests (Table 2).

Hydration age	Batches C. Paste	Batches L			Batch M	Batch H
7 days	CP	L1.3	L2.6	L3.9	M2.6	H2.6
14 days	CP	L1.3	/	/	/	/
28 days	CP	L1.3	/	/	/	/

Table 2. All batches tested with UTT

The average vertical displacement of 2 Linear Variable Differential Transformers (LVDT) was used to control the test with a rate of 15 nm/s. The LVDTs were positioned on opposite sides of the loading platens, coincident with the notched faces of the sample.

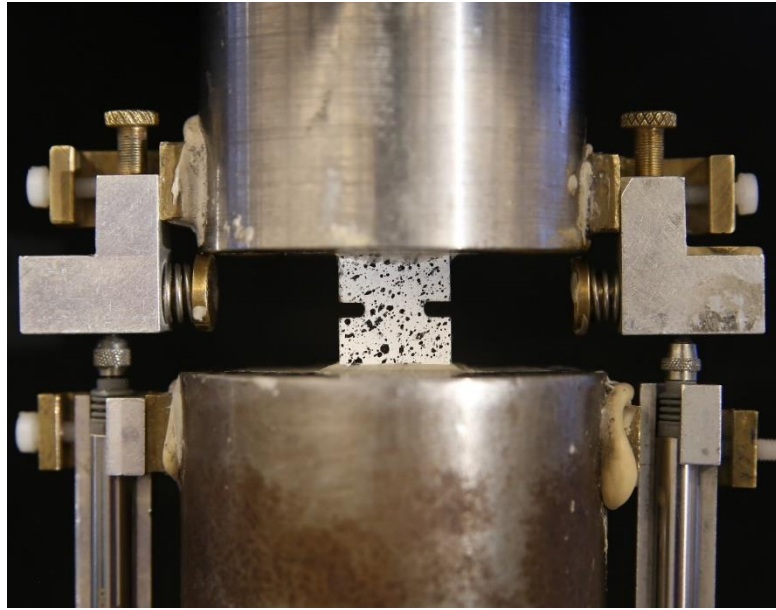


Fig. 16. Instron test setup

In the used configuration the loading platens had high rotational stiffness with respect to the bending stiffness of the specimen, therefore they don't allow rotation of the glued faces of the sample where the tension is applied [50] [51]. Prior to the test the samples were glued to the loading platens in load control to prevent pre-cracking due to the shrinkage of the pleximon glue. In Fig. 16 the configuration described above is shown. From the obtained curves of Load vs. Displacement it was possible to quantify the influence of inclusions on representative properties:

- The stiffness K_e to have information during the elastic phase;
- Tensile strength σ_t for peak information;
- Work of fracture W_f post peak behavior.

Moreover, the curve behavior could provide qualitative information on the brittleness and complexity of the rupture mechanism Fig. 17.

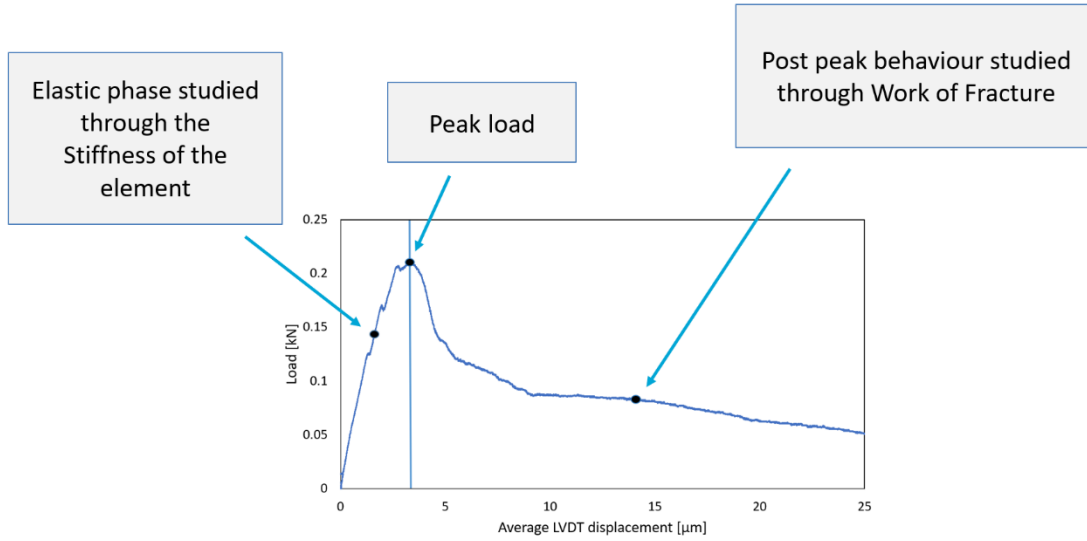


Fig. 17. Load vs. Displacement curve from a UTT.

The work generated during the tensile test to completely fracture the sample was calculated as in Equation (10):

$$W_f = \int_{u_p}^{u_f} F du \quad (10)$$

Where u_p corresponds to the elongation at the peak load and u_f to the final elongation. With regards to the elastic stiffness of the element, K_e , it was calculated simply as the quotient of the peak load and the deformation at the peak as in Equation (11):

$$K_e = \frac{F_p}{u_p} \quad (11)$$

3.5.1. Sample preparation

After the feasibility study the dimensions of samples for UTT were set to $15 \text{ mm} \times 15 \text{ mm} \times 15 \text{ mm}$ (in prevision of future lattice simulations).

Ten custom-made molds were created with a the bicomponent polymeric rubber, the procedure for one single mold is shown in Fig. 18, from each one 3 samples could be produced.

Samples were cured 28 days at $20 \text{ }^\circ\text{C}$ and 95 % of relative humidity to avoid early cracks formation due to shrinkage of cement, surface drying and thermal gradient. Cement

cracks also when surface gets dry and this can cause a reduction of volume that produces the cracks. After setting the strength of cement avoids this cracking.

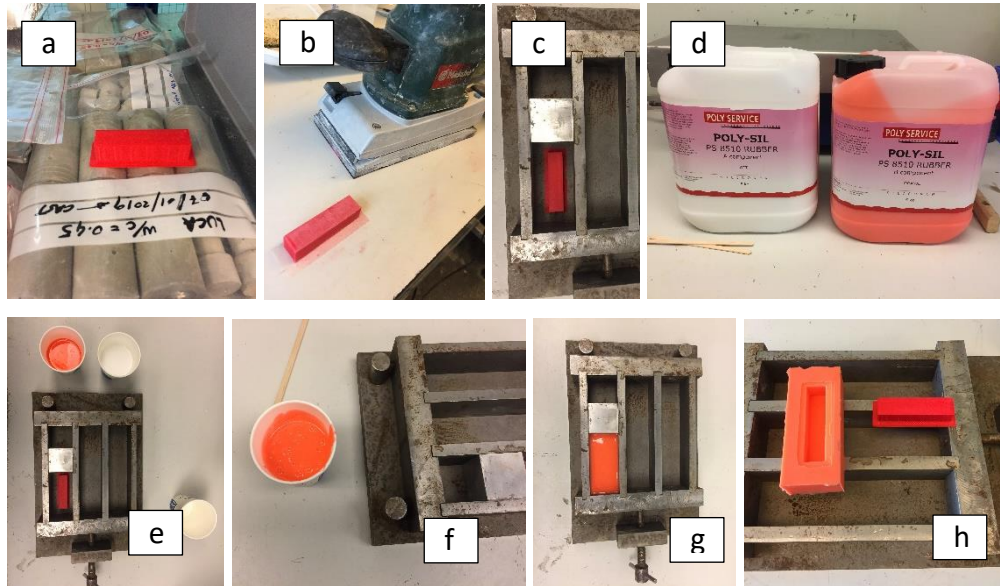


Fig. 18. In (a) the negative done with 3D printer to create the mold is shown; smothering operation (b); in (c) the negative fixed at the base of the container; Component A and B of the polymeric rubber (d); 1: 1 proportion in weight between two components (e); both component mixed until homogeneous the blend consistency and color is formed (f); pouring the mixture inside the container (g); mold extraction after 5 h approximately (h).

At the end of curing period samples were taken to the cutting room; each prismatic sample was cut into three samples and two notches for each sample were made. The sum of both notches is equal to the half of the sample cross section; in other terms $\xi = 0.5$ where $\xi = \frac{2a}{W}$, a the length of one side notch and W the cross section Fig. 19.

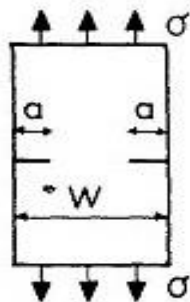


Fig. 19. Schematic representation of the samples for the UTT.

Afterwards the samples were ready to be painted to perform the digital image correlation (DIC) analysis; for this purpose, a thin layer of white painting was applied on the front face of the sample and little black random dots were drew on the same surface.

Prior to the test the samples were glued to the upper moving loading plate and successively to the lower fixed one in load control to prevent pre-cracking due to the shrinkage of the pleximon glue.

3.6 Digital image correlation

Digital Image Correlation (DIC) is a robust technique for measuring material deformation with no contact instruments need [52], [53], [54]. To track the relative displacements of material points, DIC uses image registration algorithms; typically, it compares a current image, the deformed one with the first undeformed image (reference image) [55], [54]. For each tensile test Digital Image Correlation (DIC) analysis was performed in order to track the sample surface displacements and to capture the crack pattern and crack nucleation.

The open source MATLAB program Ncorr was used for the 2D digital image correlation analysis. Prior to UTT a thin layer of white paint was applied on one side of the sample and random black dots were marked in order to perform the analysis. The resulting surface “texture” is made of randomly distributed speckles of 0.5 mm in average diameter. The digital images were acquired at 1 frame per second during the test. The digital camera used was a Canon EOS 6D, with a resolution of 20.2 megapixel and a MP-E 65mm f/2.8 1-5x Macro Photo lens.

The DIC algorithms are wholly contained within the MATLAB environment. The algorithms are optimized using C++/MEX, while the GUI is written mostly in m-code.

3.6.1. Operating principle

During the deformation images of a surface are recorded by digital photography. A digital image can be considered as a matrix of positive integers numbers each one corresponding to a pixel. Depending on the digital camera and the image acquisition electronics the range can change, for example for 8-bit system the range is $[0 - 255]$. Each pixel represents a level of surface brightness [56].

Monocular vision cannot determine the size of objects. An object that approaches or move away from the lens can produce the same sequence of images of an isotropic deformation [57]. This is one of the reasons why during the entire experiment the object is assumed planar, parallel and at a constant distance from the visual sensor.

DIC can be summarized as the tracking of a set of markers (or key points) scattered, on the surface exposed to the camera; to measure the displacements between those points the measured surface has to be “textured” before its motion. The “texture” morphology is crucial for the success of the test, for instance on a sample whose surface is covered by white painting with only one central black dot, displacements and consequently deformations would not be calculable. Also repeated/periodic patterns should be avoided because DIC software may have difficulty recognizing point location unequivocally.

The ambiguity can be removed with random textures painted by hand (for small samples) or sprayed (for bigger samples).

Some materials are naturally textured (concrete, sand, or even metals at the microstructure scale) and do not require the application of an artificial texture to be characterized [58], [59].

3.6.2. Sub-regions deformation

The reference image is partitioned into smaller regions, or subset. The deformation is assumed to be homogeneous inside each subset, and the deformed subsets points are tracked in the current image. A given point in the reference, image cannot be simply tracked in the following current images; the point needs “a signature” a single grey value is not a unique signature of a point, hence neighboring pixels values are used. Such a collection of pixel values is called a subset or window [57].

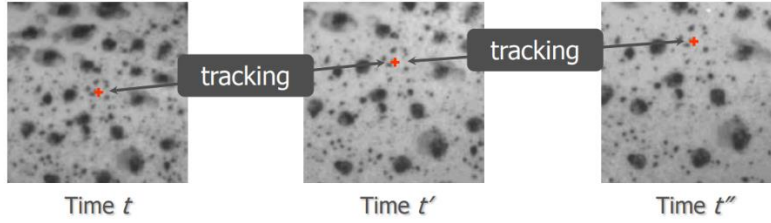


Fig. 20. Tracking subset (small but finite area) in successive current images. DIC algorithm search for the best correlation score into the grayscale intensity functions of the subset areas, at a specified location between the initial configuration, and the corresponding area of the current image [54], [55], [57].

The uniqueness of each signature is only guaranteed if the surface has a non-repetitive, isotropic, high contrast pattern (a good exposure, a constant source of light with non-shaded areas is essential provide good conditions for the analysis) [57].

The transformation of the coordinates of these points from the reference to the current configuration is constrained to a linear, first order transformation [54]:

$$\begin{aligned} x_{cur,i} &= x_{ref,i} + u_{rc} + \frac{\partial u}{\partial x_{rc}}(x_{ref,i} - x_{ref,c}) + \frac{\partial u}{\partial y_{rc}}(y_{ref,j} - y_{ref,c}) \\ y_{cur,j} &= y_{ref,j} + v_{rc} + \frac{\partial v}{\partial y_{rc}}(x_{ref,i} - x_{ref,c}) + \frac{\partial v}{\partial x_{rc}}(y_{ref,j} - y_{ref,c}) \end{aligned} \quad (12)$$

$$p = \left\{ u, v, \frac{\partial u}{\partial x}, \frac{\partial u}{\partial y}, \frac{\partial v}{\partial x}, \frac{\partial v}{\partial y} \right\} \quad (13)$$

Were $x_{ref,i}$ and $y_{ref,j}$ are the x and y coordinates of an initial reference subset point, subscripts “ c ” refer to the center of the initial reference subset, and subscripts “ $curr$ ” refer to the coordinates of a current subset point.

With u_{rc} and v_{rc} the author denotes displacements from reference to current. Equation (13) defines a generalized deformation vector p .

3.6.3. Correlation criteria

The principle of image correlation for deformation measurement is to find a displacement field (u, v) that can match the two grayscale intensity functions, at a specified location (small but finite area) between the initial configuration, and the corresponding area of the current image.

The correlation function used by the software is the normalized cross correlation (NCC):

$$C_{cc} = \frac{\sum_{Area}(f - f_m)(g - g_m)}{\sqrt{\sum_{Area}(f - f_m)^2 \sum_{Area}(g - g_m)^2}} \quad (14)$$

In Equation (14) f and g are the grayscale intensity functions respectively for the reference and for the current image, f_m and g_m correspond to the mean grayscale values of the same reference and current subset [54].

The accuracy of measurement with DIC technique can be surprisingly high. It is due to sub-pixel grey level interpolation: if a black spot with a diameter of 1 pixel is translated across a uniform white background the neighboring pixels will react to this displacement by taking a grey level value proportional to the surface of the dot overlapping this pixel. Sub-pixel interpolation makes it possible to commonly measure displacement amplitudes smaller than 0.1 pixel, and even smaller in favorable experimental conditions. To achieve this precision, great care must be taken in providing good testing conditions (mentioned above), and by using high-quality lenses and cameras [58].

3.6.4. Strain computation

Any noise in the displacement field is a magnified error in the strain fields [60] this because the strains involve the differentiation of displacement field [54]. To reduce the noise Ncorr applies a “smoothing procedure” using the algorithm proposed by Bing Pan et al [61].

$$\begin{aligned}\varepsilon_{xx} &= \frac{1}{2} \left(2 \frac{\partial u}{\partial x} + \left(\frac{\partial u}{\partial x} \right)^2 + \left(\frac{\partial v}{\partial x} \right)^2 \right) \\ \varepsilon_{xy} &= \frac{1}{2} \left(\frac{\partial u}{\partial y} + \frac{\partial v}{\partial x} + \frac{\partial^2 u}{\partial x \partial y} + \frac{\partial^2 v}{\partial x \partial y} \right) \\ \varepsilon_{yy} &= \frac{1}{2} \left(2 \frac{\partial v}{\partial y} + \left(\frac{\partial u}{\partial y} \right)^2 + \left(\frac{\partial v}{\partial y} \right)^2 \right)\end{aligned}\tag{15}$$

Then the Green-Lagrangian strains are obtained by using the four displacement gradients as in Equation (15).

3.7 Isothermal calorimetry

The isothermal calorimetry was performed in order to determine the effect of cement paste hydration in addition to HA particles. The instrument used was the TAM Air 3114/3236, Thermometric AB Fig. 21, [62], it was operating at 600 mW and $20 \pm 0.02\text{ }^\circ\text{C}$, positioned in a room conditioned at $20 \pm 2\text{ }^\circ\text{C}$ and 50% relative humidity.

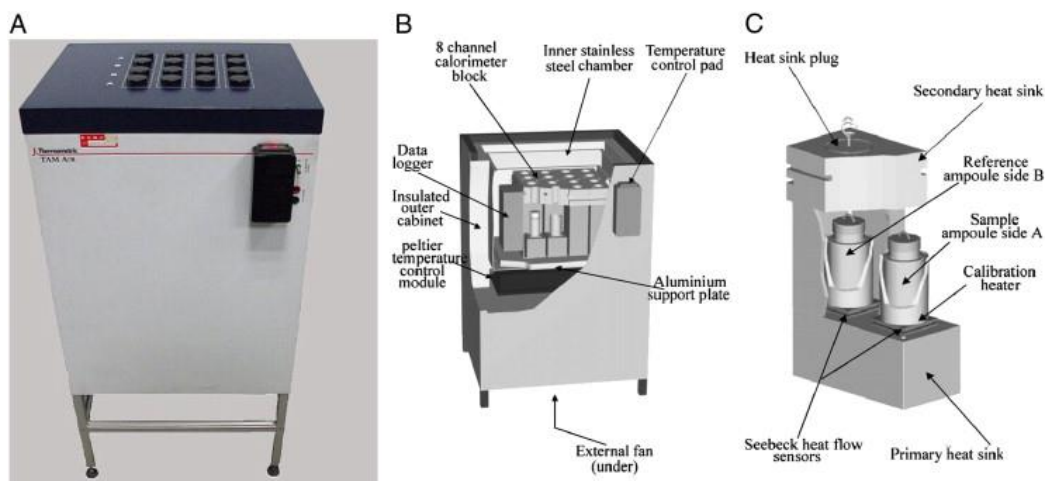


Fig. 21. Here in (A) the same isothermal calorimetry used at TU Delft Microlab for the test mentioned above. In (B) a scheme of the instrument in (C) an enlargement of one of the 8 calorimetric channels showing the twin configuration. Xi Li et al. Synthesis, crystal structure and action on Escherichia coli by microcalorimetry of copper complexes with 1,10-phenanthroline and amino acid. Journal of Inorganic Biochemistry Volume 105, Issue 1, January 2011, Pages 23-30.

Heat of hydration was recorded on the Microlab computer for 4 days at 1 min intervals. The instrument is provided with 8 channels that allow to measure until 8 samples together.

3.7.1. Sample preparation

In each 20 mL glass ampoule, a cement powdered mass of 5 g , 2.25 g of water plus additional 1.3% in mass of HA was added. One cement paste sample was used as reference for the one containing polymers. Final weight of all samples containing HA was: 7.565 g . Each composition was tested twofold. The temperature difference of the placed sample was caused by heat flow measured during the first hour.

4 Results and discussion

4.1 Bond strength of polymer-cement matrix interface

All the tested samples failed near the interface particle-cement paste. In Fig. 22 the typical failure surfaces of the bi-material samples are shown.

For both L and M, a white precipitate was observed within the polymer-cement paste

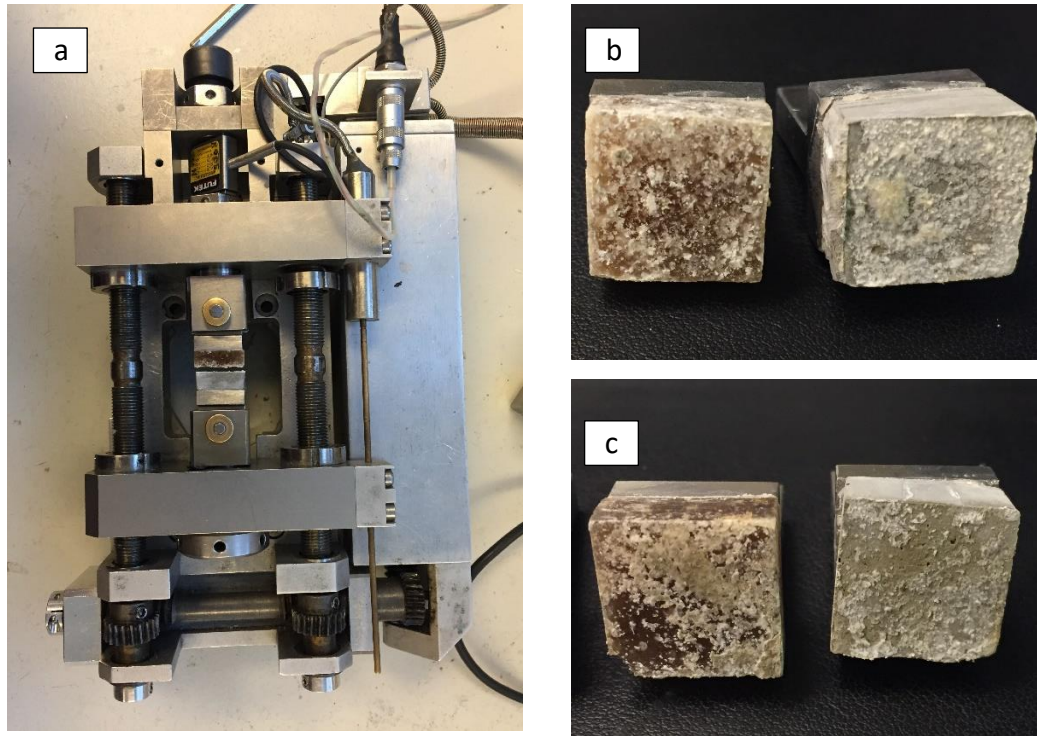
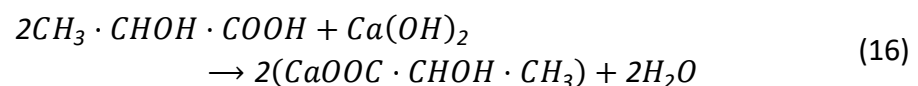


Fig. 22. Sample after test in (a) and failure surface of M in (b) and L (c) samples.

interface Fig. 22 (a) and (b). It is believed from visualization of the interface that the biopolymer was not inert in the alkaline environment of the cement paste and that calcium leachates from the biopolymer are responsible for the observed precipitate Fig. 22. The reaction in Equation (16) shows the main reaction of the lactate polymer contained into HA particles [63]. The carboxylic group contained into lactic acid interacts with calcium hydroxide $Ca(OH)_2$ of cement paste, two molecules of lactic acid will combine with one molecule of $Ca(OH)_2$ in the following manner:



Both the failure surfaces of the bi-material samples prepared from M show regular presence of the white precipitate, suggesting that the failure may have occurred within the layer of precipitate. Whereas observing the fracture surfaces of L samples, it is possible to observe that failure occurred both within the white precipitate and at the interface precipitate/polymer-cement paste.

From the visual inspection there seems to be less white precipitate in L samples compared to M. In the calculated bond strength from the uniaxial tensile test of bi-material samples are shown.

The results show markedly higher bond strength of cement paste with polymer M when compared to L. The stronger interface for M samples seems to be correlated to the higher amount of precipitate present at the interface.

Note, again, that in H specimens the polymer had de-bonded from the cementitious matrix upon de-molding. Its bond strength is therefore taken as zero.

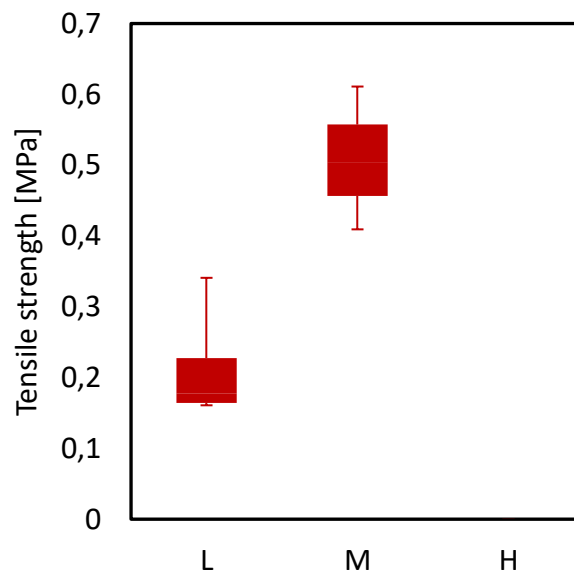


Fig. 23. Bond strength normalized to the specimen's area. Box plot with maximum value, minimum value, 25 % first quartile and 75 % for the upper one.

4.2 Micromechanical properties of the HA-Cement paste interface

The nanoindentation grid technique has been proven to provide useful unprecedented access to quantitative information about the mechanical behavior of cement pastes at the nanoscale [64], [65], [66], [67], [68].

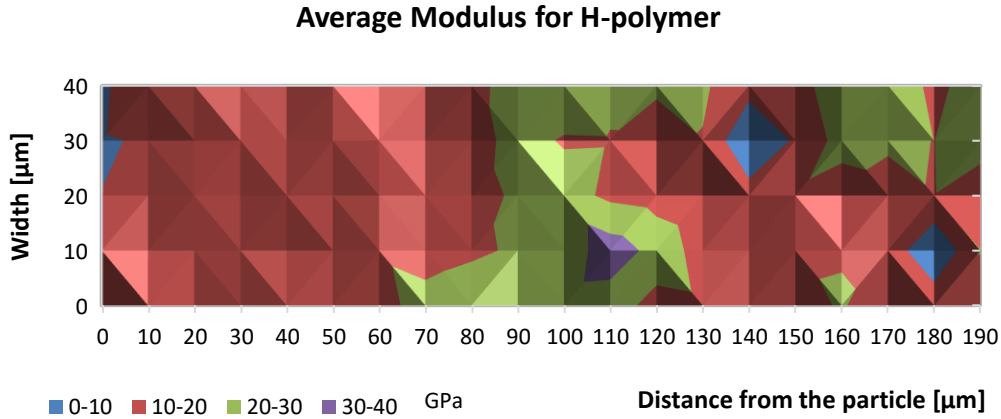


Fig. 24. H-polymer reactivity average modulus measured at 28 days with nanoindentation; colored value ranges in picture are in GPa.

The raw data were organized in a 2D isometric graph as shown in Fig. 24, Fig. 25 and Fig. 26. Each 2D isometric representation is the graphical result of a 5×20 indented grid, that means that each coordinate of the 2D graph corresponds to one coordinate of the indented grid.

In Table 3 on the first column, based on a 3×15 indents grid, the mean value of the average modulus of the cement paste is indicated; the next columns show the mean value of the different polymer at distance from the particle equal to 0 (edge of the ITZ, mean value of $[0; 0]$, $[0; 10]$, $[0; 20]$, $[0; 30]$, $[0; 40]$).

Cement Paste	L	M	H
$23.1 \pm 5.8 \text{ GPa}$	$14.8 \pm 3.7 \text{ GPa}$	$23.9 \pm 2.4 \text{ GPa}$	$11.2 \pm 1.2 \text{ GPa}$

Table 3. The first column shows the mean value of the average modulus for bulk cement paste; the other three columns the mean average modulus for different reactivity polymer at distance from the particle equal to 0 in the graph (edge of the ITZ).

To get an overall trend for the indented ITZ area, the following procedure was developed. The values of the isometric graphs can be reorganized according to five parallel segments of length $190 \mu\text{m}$ each.

At first each single 20 indents line/segment was plotted (Fig. 27 (A) polygonal line). For each line the more representative trend line with the lowest R^2 coefficient was traced (dotted line in Fig. 27 (A)). By making the mean value of lines coefficients it is possible to have information about the average trend of all the indented strip $200 \mu\text{m} \times 50 \mu\text{m}$. At last the trend line of the strip with the mean parameters was traced Fig. 27 (B).

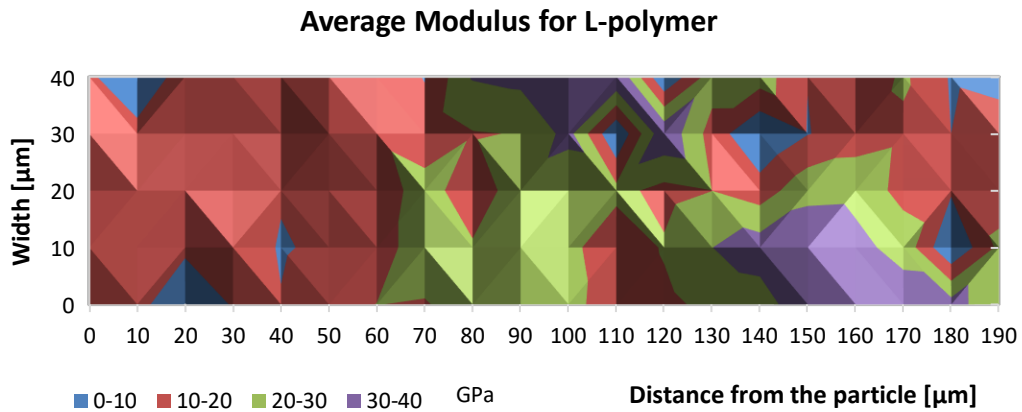


Fig. 25. L-polymer reactivity average modulus measured at 28 days with nanoindentation; colored value ranges in picture are in GPa.

Fig. 24 and Fig. 25 show the nanoindentation results of L and H polymer. In the first $75 \pm 10 \mu\text{m}$ the average Modulus values are drastically decreased by the presence of the HA particle that react with the cement matrix around it. The remaining part of the strip, from $75 \pm 10 \mu\text{m}$ to $190 \mu\text{m}$ tends to the value of the bulk cement paste Fig. 27 (B) and Fig. 28 (B).

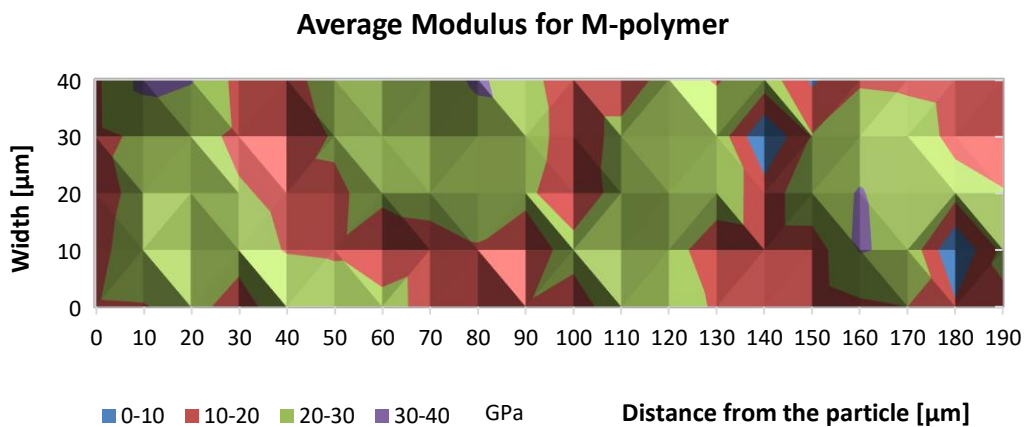


Fig. 26. M-polymer reactivity average modulus measured at 28 days with nanoindentation; colored value ranges in picture are in GPa.

It is possible to assume that the resulting values of average modulus on the Interfacial Transit Zone (ITZ) (the first $75 \pm 10 \mu\text{m}$) are the result of calcium-lactate reaction as described in Equation (16). The extension of modified cement matrix zone around the particle depends on the polymer reactivity, quantity and hydration time [63].

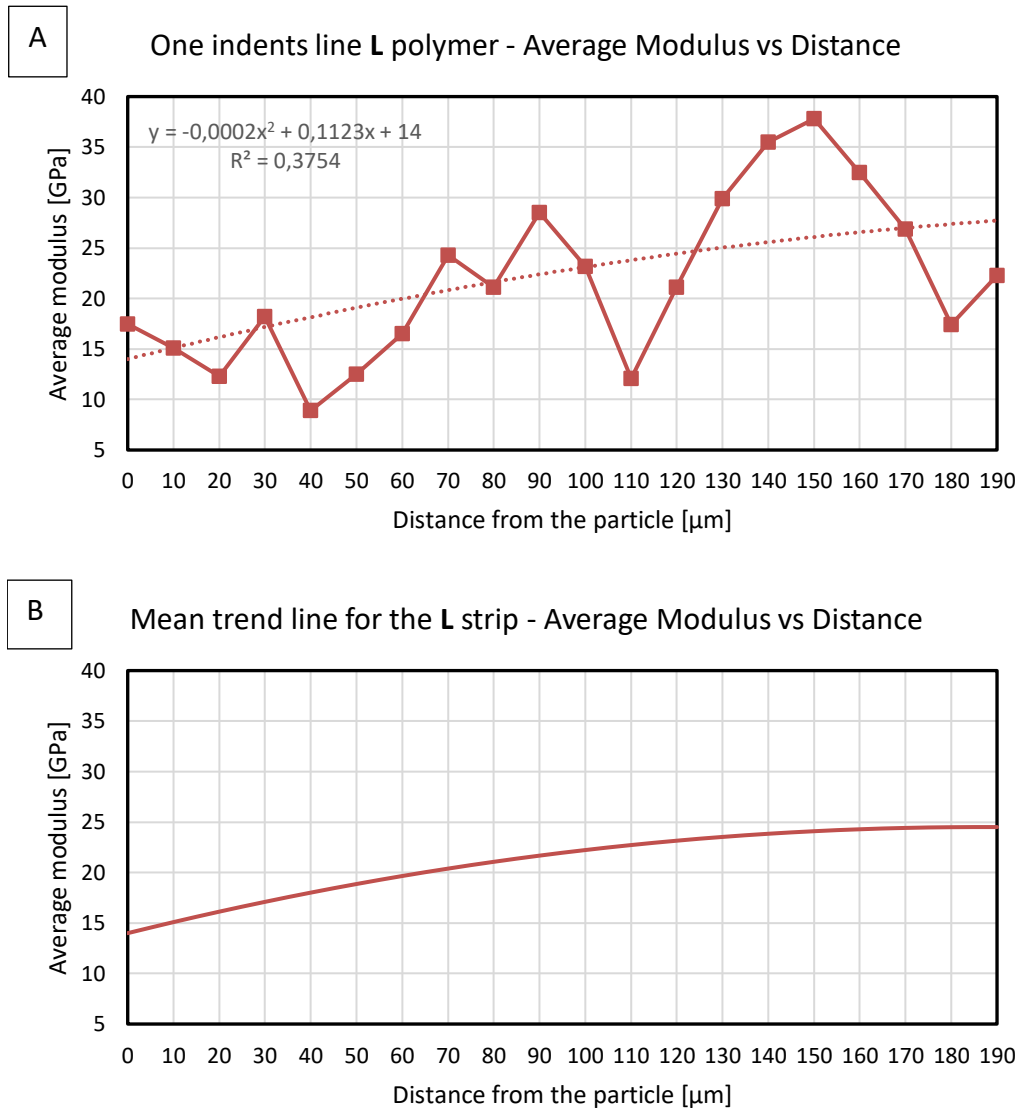


Fig. 27. Graph (A) shows the Average Modulus for one line of 20 indents and the trend line equation of L polymer. The sample was 28 days old; In (B) the mean trend line of the Average Modulus for the L strip.

For the M polymer the opposite trend was found. The indented area presents a stiffened zone around the HA particle as visible in Fig. 26 and. The mean trend line of the Average Modulus for M and H strips are shown in Fig. 28 (B).

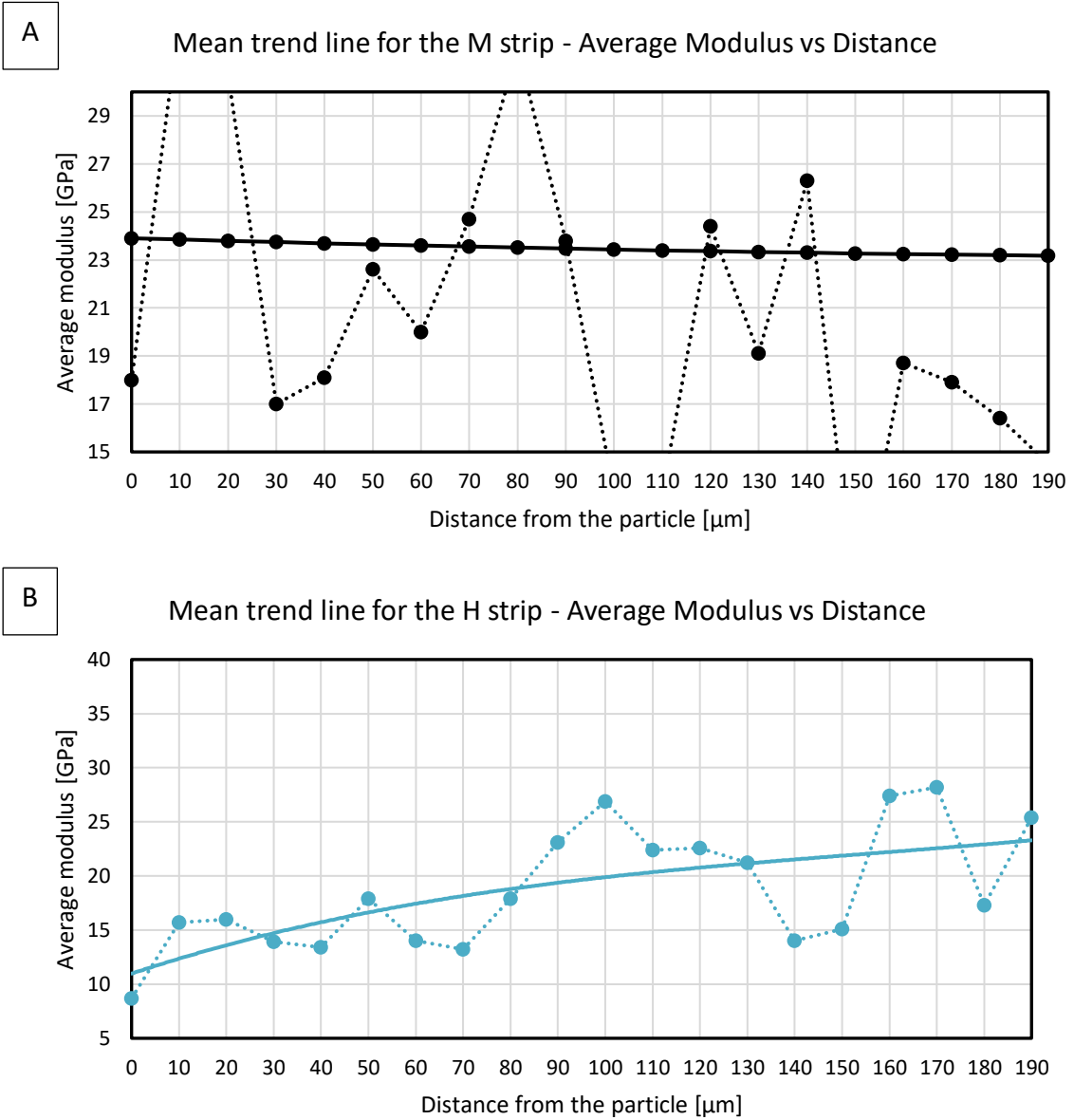


Fig. 28. Mean trend line for the M strip in the first graph (A). Mean trend line for the H strip in the second graph (B). Note that in (B) Y axes is stretched in order to appreciate the opposite curvature of the trend line.

The visual inspection, the bond strength results from 4.1 and the nanoindentation results prove that embedded lactate-based capsules cause changes into the cement paste. As schematized in Fig. 29 a precipitate part is formed all around the cement paste in contact with the particle, probably formed from the reaction of lactic acid and calcium hydroxide like in Equation (16); then a modified crown area with $75 \pm 10 \mu m$ of

extension, detected through the nanoindentation test, can be identified as the interfacial transit zone around the particle.

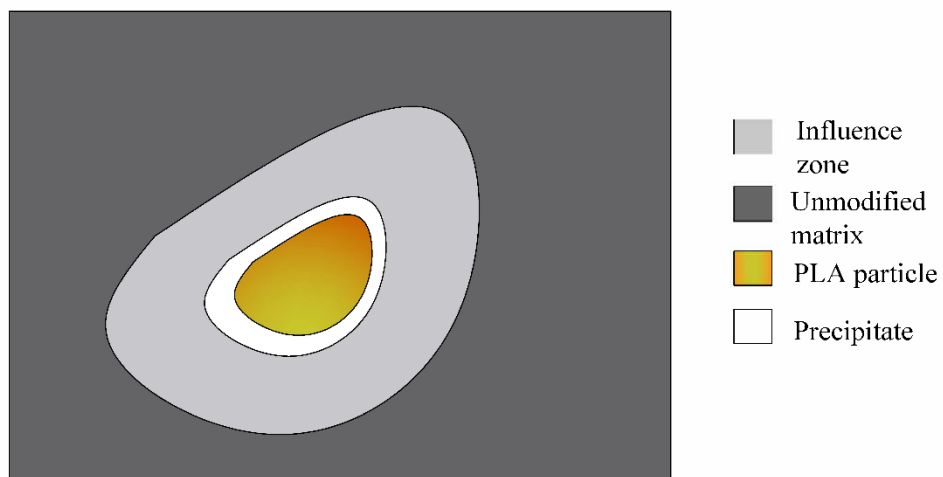


Fig. 29. Scheme of the modified cement matrix around the particle.

4.3 Isothermal calorimetry

The hydration heat of cement powder HA inclusions and water measured with TAM Air 3114/3236, Thermometric AB, gave the curves in Fig. 30.

Test recorded 4 days data with 1 min intervals. One cement paste ampoule was used as reference. Ampoules containing polymers had the same percentage in mass used in the UTT samples.

From the normalized heat of hydration Fig. 30 is possible to see that the polymers M and L have a higher peak than the reference sample consisting only of cement paste. The hydration heat recorded for the H sample is heavily influenced by the presence of the polymer: the normal peak that typically occurs in the first twelve hours is instead shifted to the 48th hour followed by a second minor peak 20 hours later. In the cumulative curve it can be noted that the H polymer after 103 h reach the same value of L and M polymer. The results were repeated on both groups of tested specimens they also provide additional proof of the reactivity of the HA particles into the cement paste.

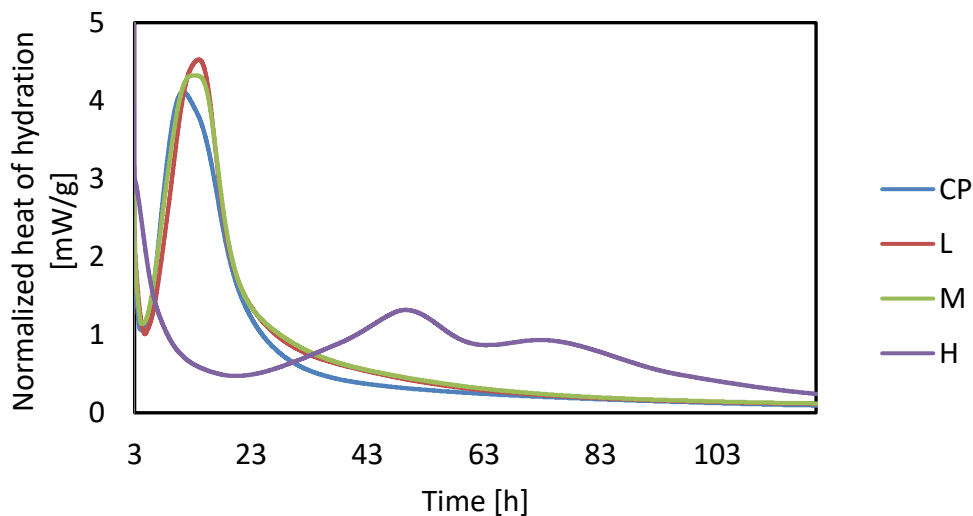


Fig. 30. Hydration heat released from HA particles mixed with cement paste. In blue the heat released from cement paste only.

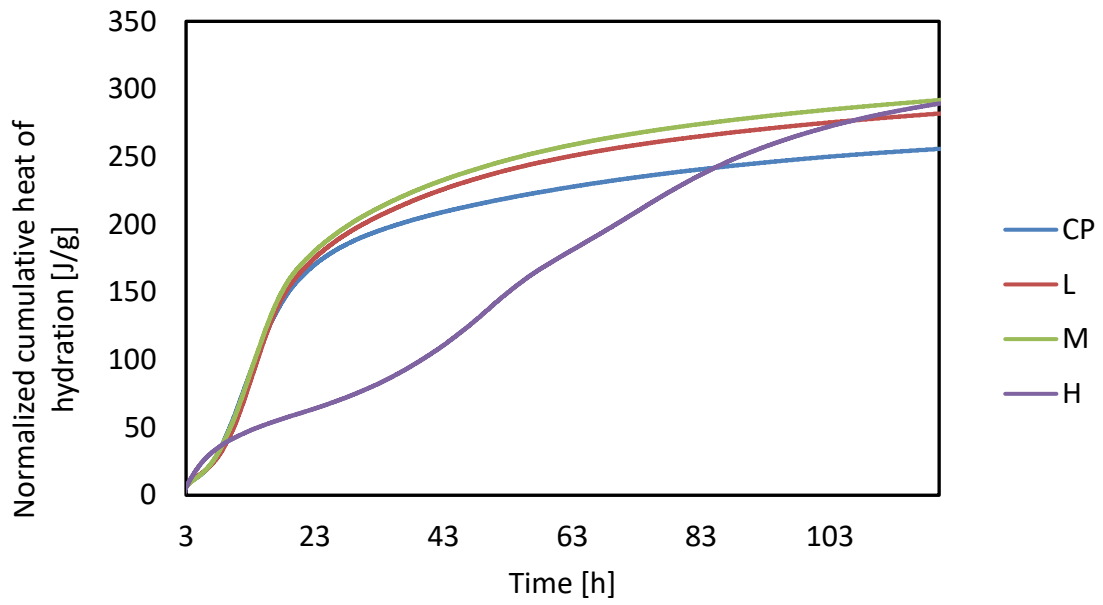


Figure 31. Normalized cumulative heat of hydration from HA particles mixed with cement paste. In blue the heat released from cement paste only; in purple the line of the H polymer that tend to rejoin the values of the other two polymer type.

4.4 Boundary conditions of UTT

In Fig. 32 and Fig. 33 a typical DIC analysis of the sample surface and corresponding curve load vs. vertical displacement, respectively, are shown.

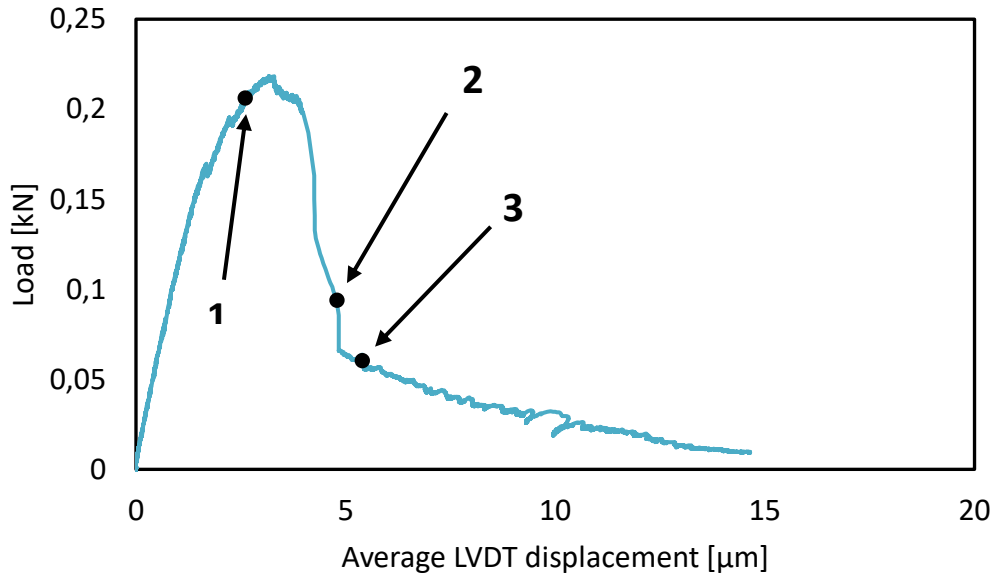


Fig. 32. Typical load-vertical displacement for the used configuration and tested samples.

The specific test configuration of fixed platens and two-notched cubes resulted in a characteristic state of stresses arising in the sample as described in [50] [51] [69]. For the majority of the tested samples, under these conditions, a crack nucleated from one of the notches first, as visible in and then continued to propagate to the other notch until a certain moment Fig. 33 (b).

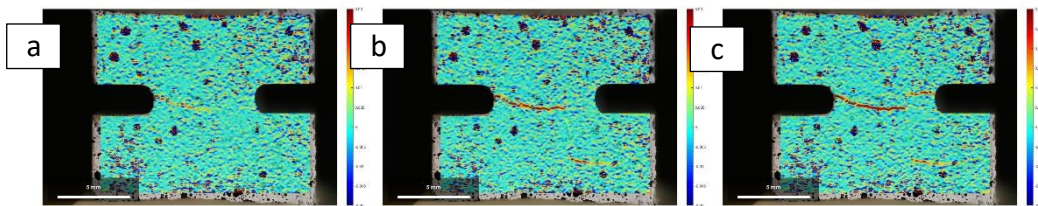


Fig. 33. (a) shows crack nucleation from the left notch, in (b) the phase corresponding to arrow 1 after the peak load in, first crack stopped (arrow 2), second crack nucleation from the right notch (arrow 3).

At this point the propagation of the first crack stopped and a new one nucleated from the opposite notch Fig. 33 (c). As the first crack propagated and the ligament area was decreased, a bending moment arise due to the restraint rotation imposed by the

rotationally fixed loading platens until the tensile stresses at the opposite notch overcame locally the tensile strength of the material.

Theoretically, the failure evolution observed in the section 5.2 (above) can be noticed in plate-like specimens in tensile regime. In that situation Fig. 34 (b) rotation platens are fixed, the condition $\theta = 0$ is valid when the stiffness of the loading platens is much bigger than the one of the samples $K_P \gg K_S$.

From the resulting load-displacement curve Fig. 34 (b), a plateau is observed between the propagation of the first crack and the nucleation of the second crack [70] [71].

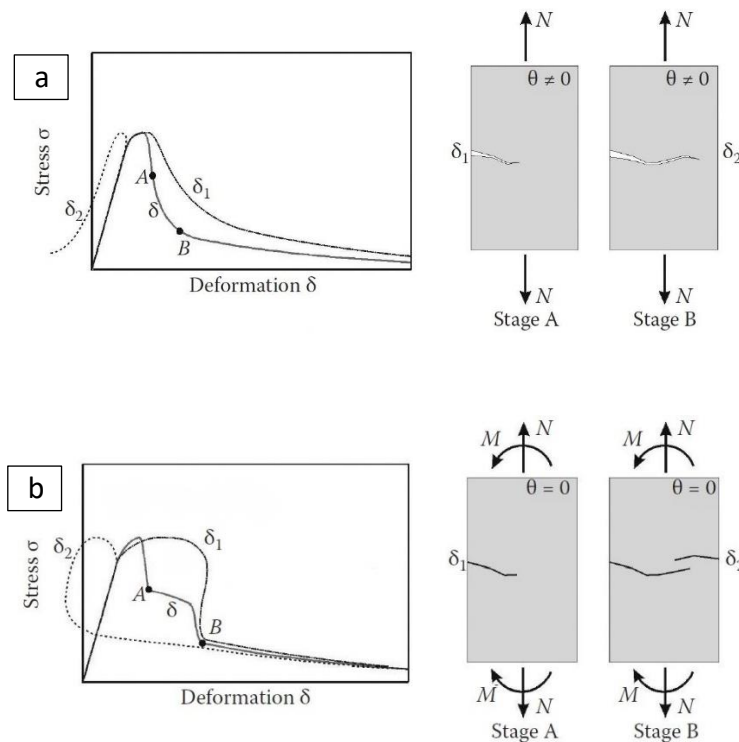


Fig. 34. Load vs. Deformation curves and different rupture mechanism in the case of free rotating platens (a) and fixed platens (b). (After Van Mier. 2004a. In Proceedings of the 5th International Conference on Fracture of Concrete and Concrete Structures FraMCoS-V) [71].

The total deformation is function of the local deformations δ_1 and δ_2 measured at opposite sides of the specimen:

$$\delta = \frac{(\delta_1 + \delta_2)}{2} \quad (17)$$

In Fig. 34 (b) the deformation δ_2 (on the opposite side of crack nucleation) change in direction unlike δ_1 causing the “wagging” in the softening part of the curve.

In the case of free rotational loading platens Fig. 34 (a), the main crack can simply propagate because no bending moment arise to stop it. There is no change in direction for δ_1 and δ_2 that can draw a smooth and gradual resulting δ in the softening regime.

In most of the tested samples this “bump” was not evident from the obtained curves. In [50] the author explain that cubical shapes of the sample resulted in a triaxial stress state, in the sense that local rotations may arise along the diagonal not aligned with the LVDT and go undetected.

4.5 Influence of hydration age on the mechanical properties

In Fig. 35, Fig. 36 and Fig. 37 the calculated K_e , σ_t and W_f are summarized for cement paste (CP) and for paste containing 1.3 % by weight of cement of polymeric particles L1.3 %. These were assumed to come from normal distributions and were tested through one-sided Grubbs outlier tests [72].

The stiffness calculated from the elastic branch of the curves load-displacement was used as an indication of the elastic properties of the studied composites Fig. 35.

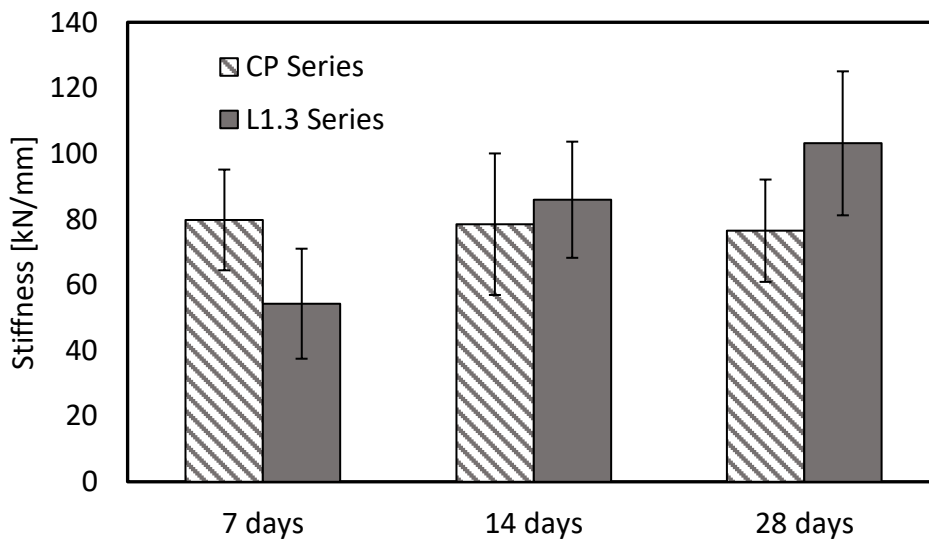


Fig. 35. Stiffness at different hydration ages.

The stiffness of cement paste sample remains more or less constant with hydration time. The cement type used in the samples was *CEM I 52.5R* which hydrates faster than normal cement because of the higher specific surface. Nevertheless, for samples containing SH capsules this was not the case. A clear increasing trend is noticeable and at 28 days the samples with HA particles present higher stiffness than the reference cement paste. The presence of the particles, which were proven to be reactive in the alkaline environment of cement paste, as shown in sub-section 4.1, seem to have modified the hydration of an influence zone around the particle; this confirms what was said in the sub-section 4.1 Bond strength of polymer-cement matrix interface: the formation of an intermediate zone that acts as a bridge between the polymer and the cement paste.

Regarding tensile strength the cement paste samples show only small increases with increasing age Fig. 36. This mild strength development after 14 days is linked to the fast

hydration of *CEM I 52.5R*, as discussed for the stiffness. The trend of tensile strength development with age results somehow unclear for *L1.3* %.

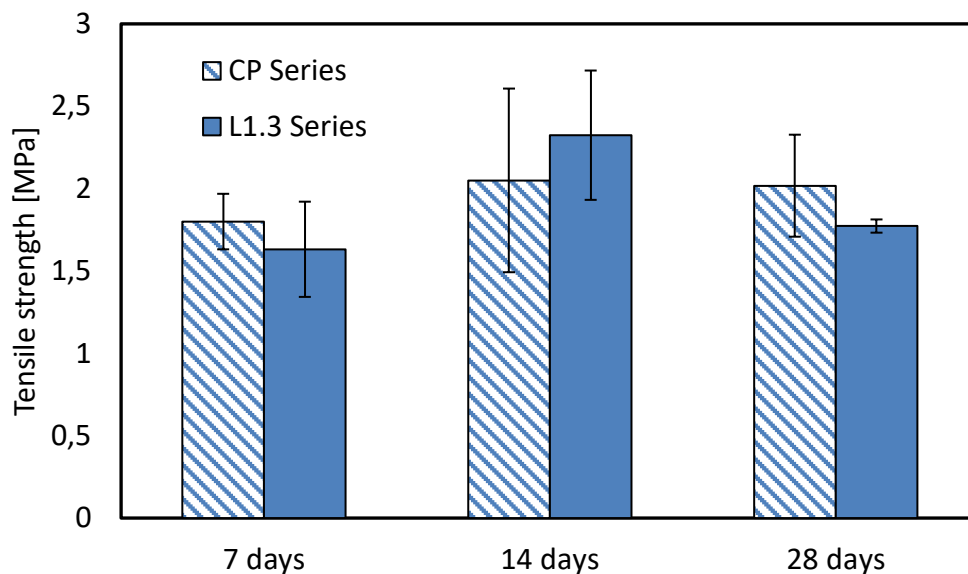


Fig. 36. Tensile strength at different hydration ages.

Overall, the strength increased mildly from 7 to 28 days (about 8 %), but an unexpected value of tensile strength was measured for 14 days, higher than that at 28 days.

At 28 days of hydration the tensile strength of *L1.3* was lower than that of CP around 3 % which overall can be translated as the particles having small impact on this property for the studied dosage.

Post peak behavior of young samples both from CP and *L1.3* presented high variability as evinced from the values of the work of fracture reported in Fig. 37. The evolution of the work of fracture for CP series is as reported for its other properties: no differences on the property value is noticeable from 14 to 28 days of hydration. On the other hand, for *L1.3* a decreasing work of fracture is evident in the same interval of time with a significant decrease of 80 % in values from 7 to 28 days.

Presumably the effect of embrittlement due to the stiffening of samples Fig. 35 with hydration was incremented by the presence of lactates contained into the HA. It is also possible to see that the work of fracture, for samples containing inclusions, generated at early ages tends to coincide with the one of only cement paste, then decrease till the minimum value corresponding to 28 days old.

In addition, supposedly the lactate particles influence the kinetics of cement hydration and/or interacts chemically with the cement in such a way that the achievement of the “final” value of the property is delayed.

Overall, cement paste and samples containing inclusions presented higher work of fracture at 28 days than the paste with 1.3 % of inclusions.

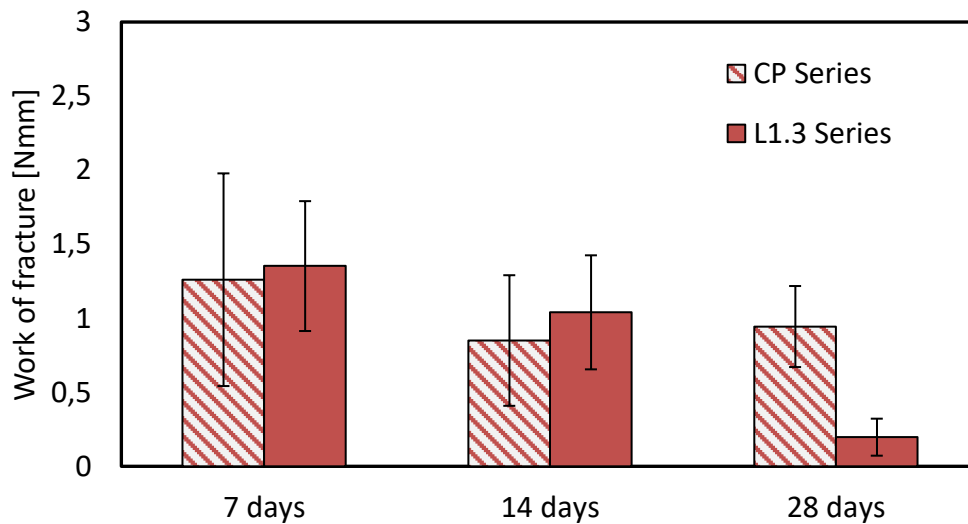


Fig. 37. Work of fracture at different hydration ages.

4.6 Influence of HA dosage on the mechanical properties

Fig. 38 and Fig. 39 show the calculated K_e , σ_t and W_f . They are summarized for cement paste (CP) and for samples containing 1.3, 2.6 and 3.9 % by weight of cement of L polymeric particles with 28 days old.

These were assumed to come from normal distributions and were tested through one-sided Grubbs outlier tests [72].

As in part expected the introduction of an increasing number of inclusions is directly proportional to the increase of work of fracture. It can be possibly explained with the idea that a major number of inclusions corresponds to the introduction of more defects inside the cement paste that leads to more tortuous crack paths. Longer paths with more or less constant strength applied translates to higher work Fig. 38.

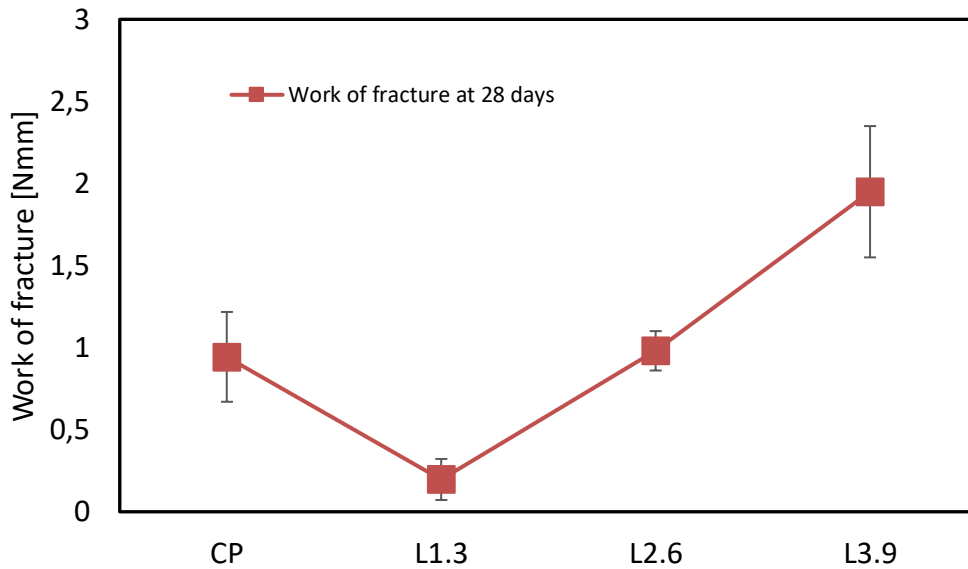


Fig. 38. Work of fracture at 28 days, samples with increasing quantity of HA inclusions.

In picture Fig. 39 is possible to notice that the two correlated variables: tensile strength and element stiffness follow the same trend, excepted *L1.3*, with some differences in the magnitude of errors; bigger error bars are present into the element stiffness line because of the elongation at the peak error contribution.

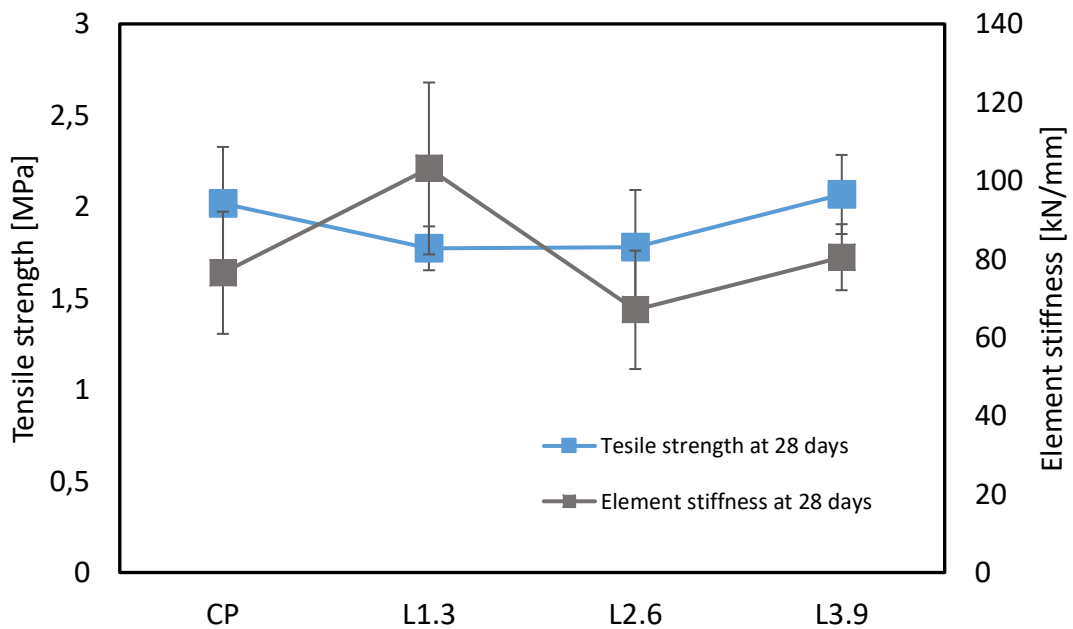


Fig. 39. Tensile strength at 28 days, samples with increasing quantity of HA inclusions.

4.7 Influence of polymer reactivity on mechanical properties

Fig. 39 and Fig. 40, Fig. 41 show the calculated K_e , σ_t and W_f . They are summarized for cement paste (CP) and for samples containing the fixed amount of 2.6 % by weight of cement for L , M and H polymer inclusions type, all 28 days old. It should be noted that each reactivity presents differently sized particles and different shapes, therefore only the stiffness of the element is significantly comparable.

These were assumed to come from normal distributions and were tested through one-sided Grubbs outlier tests [72].

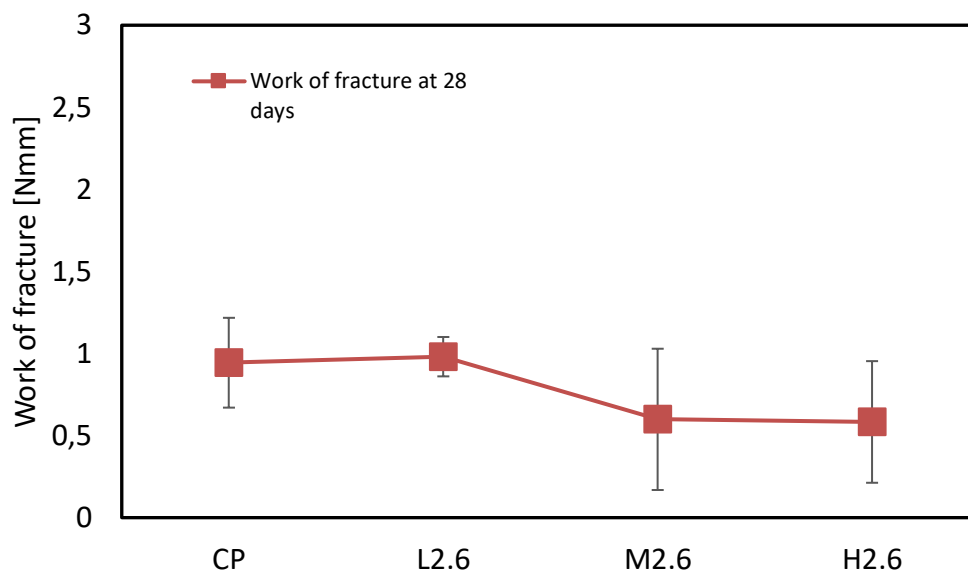


Fig. 40. Work of fracture at 28 days, for samples with different HA inclusions reactivity.

The work of fracture keeping constant the quantity of HA and hydration age stays mostly unchanged, Fig. 40.

The change of polymer reactivity seems to have no influence also in tensile strength and stiffness. Only M reactivity shows a slight increase in strength that exceed the cement paste value. The increase in M can presumably be correlated with the higher bond strength manifested into the tensile test sub-section 4.1.

In the same way of Fig. 39 both tensile strength and stiffness (not independent quantities) follow the same trend Fig. 41.

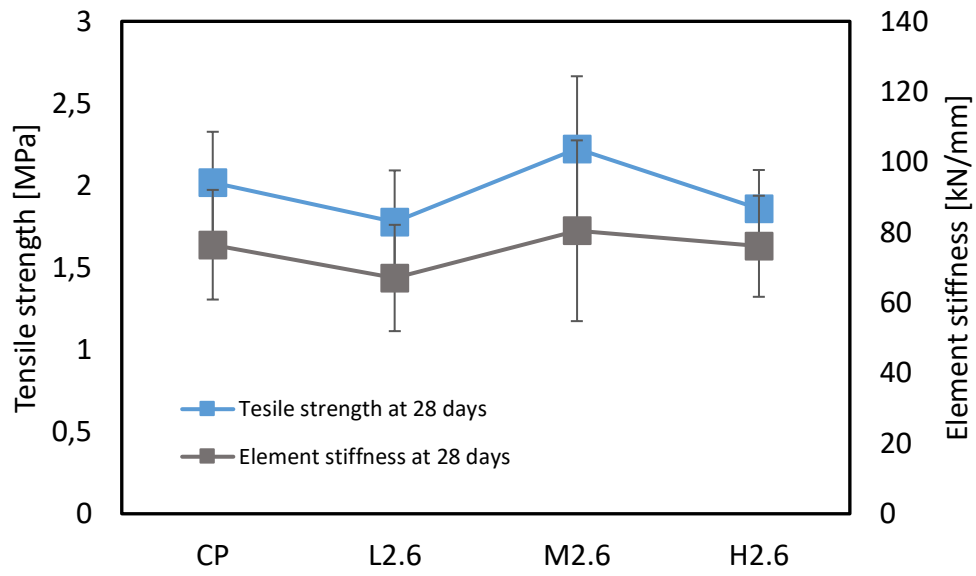


Fig. 41. Tensile strength and element stiffness at 28 days, for samples with different HA inclusions reactivity.

5 Conclusions and future developments

Some conclusions can be derived from the work presented in this study. Regarding the influence of lactate-derived self-healing particles on the fracture behavior of cement paste:

- The lactate-derived HA particles L and M show different levels of reactivity in the alkaline environment of cement paste, resulting in different bond strengths with cement paste. A failure within the layer of precipitates between polymer and cement paste seems to yield higher bond strength than a failure along the interface cement paste-polymer/precipitate.
- From the comparison between the development in time of stiffness, tensile strength and work of fracture of plain and self-healing cement pastes is suggested that the HA particles influence the hydration kinetics of cement or interact chemically with the surrounding paste over time.
- From the hydration age study on the L polymer, it was possible to notice that at 28 days the addition of HA particles resulted in negligible decrease in the tensile strength of 3 % and dramatically reduction of the work of fracture at around 80 % an increase in stiffness of 42 %,
- The study on the different quantity revealed that by changing quantity from 1.3 % to 3.9 % the work of fracture increased 9.8 times, negligible changes in the tensile strength and the stiffness of the element. With respect to the cement paste (with no inclusions in it) work of fracture increased by 2.1 times, it is possible to assumed that such behavior is the result of defects introduction represented by the SH particles.

The isothermal calorimetry provides additional proof of the reactivity between HA particles components and cement paste.

The nanoindentation results prove that the embedded lactate-based capsules cause changes into the cement paste, and an interfacial transit zone of $75 \pm 10 \mu m$ around the particle can be identified.

6 References

1. Zwaag, Sybrand van der. *Self Healing Materials - An Alternative Approach to 20 Centuries of Materials Science*. Delft : Springer, 2007.
2. M.Coronado, T.Blanco, N.Quijorna, R.Alonso-Santurde, A.Andrés. 7 - Types of waste, properties and durability of toxic waste-based fired masonry bricks. *Eco-Efficient Masonry Bricks and Blocks*. s.l. : DOI, 2015, p. 129-188.
3. ScienceDirect. [Online] [Riportato: 17 June 2019.] <https://www.sciencedirect.com/search/advanced?qs=concrete%20AND%20heal&authors=NOT%20heal&tak=heal&show=25&sortBy=relevance&years=2002&lastSelectedFacet=years>.
4. Mario de Rooij, Nele De Belie, Kim Van Tittelboom, Erik Schlangen. *Self-Healing Phenomena in Cement-Based Materials*. s.l. : RILEM, Springer, 2013.
5. *2013 Report Card for America's Infrastructure*. Engineers, American Society of Civil. 2013, Infrastructure Report Card.
6. *Corrosion of Highway Bridges: Economic Impact and Control Methodologies*. Thompson, Mark Yunovich and Neil G. 1, 2013, Concrete International, Vol. 25, p. 52-57.
7. *LIFE-CYCLE COST ANALYSIS FOR LARGE SEGMENTAL BRIDGES*. Freyermuth, C L. 2, 2001, Concrete International, Vol. 23, p. 89-95.
8. *LIFE-CYCLE COST APPROACH TO BRIDGE MANAGEMENT IN THE NETHERLANDS*. Klatter, H E e Van Noortwijk, J M. Orlando, Florida : s.n., 2003. 9th International Bridge Management Conference.
9. DTI. *Construction statistics annual report 2006*. London : TSO, 2006.
10. *A review of self-healing concrete*. Nele De Belie, Elke Gruyaert, Abir Al-Tabbaa, Paola Antonaci, Cornelia Baera, Diana Bajare, Aveline Darquennes, Robert Davies, Liberato Ferrara, Tony JefJefferson, et all. 2018, Advanced Materials Interfaces.
11. *Self-healing in cementitious materials: Materials, methods and service conditions*. Haoliang Huang, Guang Ye, Chunxiang Qian, and Erik Schlangen. 2016, Materials & Design, Vol. 92, p. 499–511.
12. *Visualized tracing of crack self-healing features in cement/microcapsule system with X-ray microcomputed tomography*. Guohao Fang, Yuqing Liu, Shaofeng Qin, Weijian Ding, Jianchao Zhang, Shuxian Hong, Feng Xing, and Biqin Dong. 2018, Construction and Building Materials, Vol. 179, p. 336–347.
13. *Selfhealing efficiency of cementitious materials containing tubular capsules filled with healing agent*. Kim Van Tittelboom, Nele De Belie, Denis Van Loo, and Patric Jacobs. 4, 2011, Cement and Concrete Composites, Vol. 33, p. 497–505.

14. *The efficiency of self-healing cementitious materials by means of encapsulated polyurethane in chloride containing environments.* Mathias Maes, Kim Van Tittelboom, and Nele De Belie. 2014, *Construction and Building Materials*, Vol. 71, p. 528–537.
15. *The efficiency of self-healing concrete using alternative manufacturing procedures and more realistic crack patterns.* Kim Van Tittelboom, Eleni Tsangouri, Danny van Hemelrijck, Nele De Belie. 2015, *Cement and Concrete Composites*, Vol. 57, p. 142–152.
16. *Waterproof performance of concrete: A critical review on implemented approaches.* Nasiru Zakari Muhammad, Ali Keyvanfar, Muhd Zaimi Abd Majid, Arezou Shafaghat, Jahangir Mirza. 2015, *Construction and Building Materials*, Vol. 101, p. 80–90.
17. *Tests and methods of evaluating the self-healing efficiency of concrete: A review.* al., Nasiru Zakari Muhammad et. 2016, *Construction and Building Materials* , Vol. 112, p. 1123-1132.
18. *Permeability of cracked concrete.* C. M. Aldea, S. P. Shah, A. Karr. 1999, *Materials and Structures*, Vol. 32, p. 370-376 .
19. *Investigation of self-healing of cracks in polymers.* Yu. M. Malinskii, V. V. Prokopenko, N. A. Ivanova, V. A. Kargin. 2, 1970, *Polymer Mechanics*, Vol. 6, p. 240–244.
20. *Is concrete healing really efficient? A review.* Sidiq, Amir, Gravina, Rebecca e Giustozzi, Filippo. 2018, *Construction and Building Materials*, Vol. 205, p. 257–273.
21. *Development of Engineered Self-Healing and Self-Repairing Concrete-State-of-the-Art Report.* Hirozo Mihashi, Tomoya Nishiwaki. 5, 2012, *Journal of Advanced Concrete Technology*, Vol. 10 , p. 170-184.
22. *Self-Healing Phenomena in Cement-Based Materials.* al., M. de Rooij et. 2013, *RILEM*, Vol. 11, p. 65–117.
23. *Autogenous healing: a concrete miracle?* Neville, A. 11, s.l. : American Concrete Institute (ACI), 2002, *Concrete International*, Vol. 24.
24. *WATER PERMEABILITY AND AUTOGENOUS HEALING OF CRACKS IN CONCRETE.* Edvardsen, C. 4, 1999, *ACI Materials Journal*, Vol. 96, p. 448-454.
25. *State-of-the-Art Report on Control of Cracking in Early Age Concrete.* Mihashi, Hirozo e Leite, João Paulo de B. 2, 2004, *Journal of Advanced Concrete Technology*, Vol. 2, p. 141-154.
26. *Most recent advances in the field of self-healing cementitious materials.* Van Tittelboom, K., et al. 2013. *ICSHM 2013: Proceedings of the 4th International Conference on Self-Healing Materials.*
27. Sangadji, Senot e Schlangen, Erik. Feasibility and potential of prefabricated porous concrete as a component to make concrete structures self-healing. *International RILEM Conference on Advances in Construction Materials Through Science and Engineering.* s.l. : RILEM Publications SARL, 2011, p. 553 - 559.

28. *Encapsulation Technology and Techniques in Self-Healing Concrete*. Souradeep, Gupta e Kua, Harn Wei. 12, December 2016, Journal of Materials in Civil Engineering, Vol. 28.
29. *Matrix cracking repair and filling using active and passive modes for smart timed release of chemicals from fibers into cement matrices*. Dry, Carolyn. 2, 1994, Vol. 3.
30. *Removal of chemical and microbiological contaminants from domestic greywater using a recycled vertical flow bioreactor (RVFB)*. Gross, Amit, Kaplana, Drora e Baker, Katherine. 1, 2007, Ecological engineering, Vol. 3, p. 107–114.
31. *Use of bacteria to repair cracks in concrete*. Tittelboom, Kim Van, et al. 1, 2010, CEMENT AND CONCRETE RESEARCH, Vol. 40, p. 157-166.
32. Krelani, Visar. *Self-healing capacity of cementitious composites*. Department of Civil and Environmental Engineering - Structural, Earthquake and Geotechnical Engineering : POLITECNICO DI MILANO, 2015.
33. *Self-Healing in Cementitious Materials - A Review*. Tittelboom, Kim Van e Belie, Nele De. 6, May 2013, materials, Vol. 6, p. 2182-2217.
34. *Microbial carbonate precipitation in construction materials: a review*. De, Muynck Willem, De, Belie Nele e Willy, Verstraete. 2, 2010, ECOLOGICAL ENGINEERING, Vol. 36, p. 118-136.
35. *Synthetic biology for the development of bio-based binders for greener construction materials*. Echavarri-Bravo, Virginia, Eggington, Ian e Horsfall, Louise E. 2, 2019, Cambridge University Press, Vol. 9, p. 474-485.
36. *Microbial cementation of ureolytic bacteria from the genus Bacillus: a review of the bacterial application on cement-based materials for cleaner production*. 15, April 2015, Journal of Cleaner Production, Vol. 93, p. 5-17.
37. *Microbial healing of cracks in concrete: a review*. Joshi, Sumit, et al. 11, November 2017, Journal of Industrial Microbiology & Biotechnology, Vol. 44, p. 1511–1525.
38. *Exploration on the biotechnological aspect of the ureolytic bacteria for the production of the cementitious materials--a review*. K1, Sarayu, NR, Iyer e AR, Murthy. 5, s.l. : US National Library of Medicine National Institutes of Health, March 2014 , Vol. 72, p. 2308-23.
39. *Enhanced crack closure performance of microbial mortar through nitrate reduction*. Erşan, Yusuf Çağatay, et al. s.l. : Elsevier, 2016, Cement and concrete composites, Vol. 70, p. 159-170.
40. *Bacterial carbonate precipitation improves the durability of cementitious materials*. Muynck, Willem De, et al. 7, 2008, Cement and concrete research, Vol. 38, p. 1005-1014.
41. *Recent advances on self healing of concrete*. Schlangen, E., et al. [a cura di] FraMCoS 7. Seul : s.n., 2010. Fracture Mechanics of Concrete and Concrete Structures. ISBN 978-89-5708-180-8.

42. *Application of bacteria as self-healing agent for the development of sustainable concrete.* Jonkers, Henk M., et al. 2, 2010, *Ecological Engineering*, Vol. 36, p. 230-235.
43. *Experimental and numerical study of crack behavior for capsule-based self-healing cementitious materials.* Lv, Le-Yang, et al. 15, December 2017, *Construction and Building Materials*, Vol. 156, p. 219-229.
44. *An In-Situ X-Ray Microtomography Study of Split Cylinder Fracture in Cement-Based Materials.* Landis, S. C. de WolskiJ. E. BolanderE. N. 7, September 2014, *Experimental Mechanics*, Vol. 54, p. 1227–1235.
45. *A technique to measure three-dimensional work-of-fracture of concrete in technique.* Landis EN, Nagy EN, Keane DT, Nagy G. 6, 1999, *Eng. Mech.*, Vol. 125, p. 599–605.
46. *Cement - Part 1: Composition, specifications and conformity criteria for common cements.* 197-1, BS/EN. 2011. 91.100.10.
47. Renee Mors, Henk Jonkers. Effect on concrete surface water absorption upon addition of lactate derived agent. *Coatings*. 7, 2017, Vol. 4, 51.
48. Warren Oliver, George Pharr. An improved technique for determining hardness and elastic modulus using load and displacement sensing indentation experiments. *Materials Research*. 1564-1583, 1992, Vol. 7, 6.
49. Karen Scrivener, Ruben Snellings, and Barbara Lothenbach. *A Practical Guide to Microstructural Analysis of Cementitious Materials*. s.l. : Taylor & Francis Group, 2016. p. 353-415.
50. J.G.M., van Mier. *Fracture Propagation in Concrete under Complex Stress*. [aut. libro] Swartz S.E. Shah S.P. *Fracture of Concrete and Rock*. New York, NY : Springer, 1989.
51. JGM Van Mier, MB Nooru-Mohamed. *Fracture of concrete under tensile and shear-like loadings*. [aut. libro] H. Takahashi, FH Wittmann H. Mihashi. *Fracture Toughness and Fracture Energy-Test Methods for Concrete and Rock*. Rotterdam : s.n., 1989, p. 549–516.
52. *Digital Imaging Techniques In Experimental Stress Analysis*. Peters, W. H. e Ranson, W. F. 3, June 1982, *Optical Engineering* , Vol. 21.
53. *Applications of digital-image-correlation techniques to experimental mechanics*. Chu, T. C., Ranson, W. F. e Sutton, M. A. 3, 1985, *Experimental Mechanics*, Vol. 25, p. 232–244.
54. *Ncorr: Open-Source 2D Digital Image Correlation*. Blaber, J., Adair, B. e Antoniou, A. 6, 2015, *Experimental Mechanics*, Vol. 55, p. 1105–1122.
55. *Digital image correlation using Newton-Raphson method of partial differential correction*. Bruck, H. A., et al. 3, 1989, *Experimental Mechanics*, Vol. 29, p. 261–267.
56. SU, C. e ANAND, L. *A new digital image correlation algorithm for whole-field displacement measurement*. Massachusetts Institute of Technology, Cambridge, MA 02139, USA : Department of Mechanical Engineering.

57. correlatedsolutions. <http://www.correlatedsolutions.com>. *2D Image Correlation*. [Online] 2018.
58. EikoSim. <https://eikosim.com/en/technical-post-en/digital-image-correlation-the-basics/>. *Digital Image Correlation – The basics*. [Online]
59. Byrne, Elisha e Lovaas, Nicholas. *Speckle Pattern Fundamentals*. s.l. : correlated solutions, 2018. <https://www.correlatedsolutions.com/support/index.php?/Knowledgebase/Article/View/80/1/speckle-pattern-fundamentals>.
60. *On the numerical differentiation problem of noisy signal*. Dhaou, O., et al. s.l. : IEEE International Conference on Automation, Control, Engineering and Computer Science, 2016.
61. Pan, Bing, et al. Digital image correlation using iterative least squares and pointwise least squares for displacement field and strain field measurements. *Optics and Lasers in Engineering*. July–August 2009, Vol. 47, 7-8, p. 865-874.
62. *Synthesis, crystal structure and action on Escherichia coli by microcalorimetry of copper complexes with 1,10-phenanthroline and amino acid*. Li, Xi, et al. 1, 2011, Journal of Inorganic Biochemistry, Vol. 105, p. 23-30.
63. *Effect of lactic acid on the hydration of portland cement*. N. B. Singh, Smt. S. Prabha, A. K. Singh. 4, 1986, Cement and Concrete Research, Vol. 16, p. 545-553.
64. *On the use of nanoindentation for cementitious materials*. G. Constantinides, F.J. Ulm, K. Van Vliet. 3, 2003, Mat. Struct, Vol. 36, p. 191-196.
65. *The effect of two types of C-S-H on the elasticity of cement-based materials: Results from nanoindentation and micromechanical modeling*. Constantinides, G. e Ulm, F.J. 1, 2004, Cement and Concrete Research, Vol. 34, p. 67-80.
66. *Surface roughness criteria for cement paste nanoindentation*. Miller, Mahalia, et al. 4, April 2008, Cement and Concrete Research, Vol. 38, p. 467-476.
67. *The nanogranular behavior of C–S–H at elevated temperatures (up to 700 °C)*. DeJong, M.J. e Ulm, F.J. 1, January 2007 , Cement and Concrete Research, Vol. 37, p. 1-12.
68. *Statistical indentation techniques for hydrated nanocomposites: concrete, bone, and shale*. F.J. Ulm, M. Vandamme, C. Bobko, J.A. Ortega, K. Tai, C. Ortiz. 9, September 2007, Journal of the American Ceramic Society, Vol. 90, p. 2677-2692.
69. Hordijk, DA. *Local approach to fatigue of concrete*. Delft University of Technology : doctoral thesis, 1991.
70. Mier, J. G. M. Van. *Fracture Processes of Concrete*. s.l. : CRC Press, 1996.
71. Mier, G.M. van. *Fracture of Concrete in Tension. Concrete fracture a multiscale approach*. s.l. : CRC Press, 2013.

72. *Procedures for detecting outlying observations in samples.* Grubbs, Frank E. Aberdeen : Technometrics, 1969, UT. S. Army Aberdeen Research and Development Center .

73. *Reinforcement corrosion in concrete structures, its monitoring and service life prediction - a review.* Ahmad, Shamsad. Issue 4-5 SPEC, 2003, Cement and Concrete Composites, Vol. 25, pp. 459-471.